

# Microscopic description of quadrupole-octupole coupling in neutron-rich actinides and superheavy nuclei with the Gogny-D1M energy density functional

R. Rodríguez-Guzmán\*

*Department of Physics, Kuwait University, Kuwait*

L.M. Robledo

*Center for Computational Simulation, Universidad Politécnica de Madrid,  
Campus Montegancedo, 28660 Boadilla del Monte, Madrid, Spain and*

*Departamento de Física Teórica and CIAFF, Universidad Autónoma de Madrid, 28049-Madrid, Spain<sup>†</sup>*

(Dated: April 19, 2021)

The interplay between quadrupole and octupole degrees of freedom is discussed in a series of neutron-rich actinides and superheavy nuclei with  $92 \leq Z \leq 110$  and  $186 \leq N \leq 202$ . In addition to the static Hartree-Fock-Bogoliubov approach, dynamical beyond-mean-field correlations are taken into account via both parity restoration and symmetry-conserving Generator Coordinate Method calculations based on the Gogny-D1M energy density functional. Physical properties such as correlation energies, negative-parity excitation energies as well as reduced transition probabilities  $B(E1)$  and  $B(E3)$  are discussed in detail. It is shown that, for the studied nuclei, the quadrupole-octupole coupling is weak and to a large extent the properties of negative parity states can be reasonably well described in terms of the octupole degree of freedom alone.

PACS numbers: 21.60.Jz, 27.70.+q, 27.80.+w

## I. INTRODUCTION

All over the nuclear chart, the majority of the spherical and/or quadrupole-deformed ground states are reflection-symmetric. However, in regions with given proton and/or neutron numbers the spatial reflection symmetry is broken spontaneously and octupole-deformed ground states are favored energetically [1]. Octupole deformation is also well known to affect the outer fission barriers of atomic nuclei and is the collective variable associated to cluster radioactivity (see, for example, [2–5]). The search for signatures of octupole correlations has remained an active research field over the years [6–16]. Previous experiments have found evidence for octupole-deformed ground states in  $^{144,146}\text{Ba}$  [12, 13] and  $^{222,224}\text{Ra}$  [14, 15] or measured the  $E1$  strength in  $^{228}\text{Th}$  [16]. Furthermore, a correlation between the Schiff moment [17] and octupole deformation has been found [18] suggesting that octupole-deformed nuclei might represent the best candidates for atomic electric dipole moment measurements.

From a theoretical point of view, various models and approaches have already been employed to study the properties of octupole collectivity. Among them we can mention the studies of octupole shapes carried out using the macroscopic-microscopic (MM) approach [19–23] or the use of the Interacting Boson Model (IBM) [24–27] with parameters determined using fermion-to-boson mapping procedures starting from mean-field potential energy surfaces (MFPEs), obtained with relativistic and

non-relativistic energy density functionals (EDFs).

Microscopic non-relativistic and relativistic approaches, both at the mean-field level and beyond, have been widely used to study octupole correlations [28–51]. Those microscopic studies include global surveys looking for octupole deformed mean field ground states in even-even nuclei [45–51]. In addition, properties of dynamic octupole correlations have been analyzed in large scale beyond-mean-field calculations carried out for even-even nuclei and using several parametrizations of the Gogny [52] EDF [50, 51]. The results of those calculations indicate that not only static octupole deformation but also dynamical beyond-mean-field octupole correlations have a sizeable impact on physical observables.

The interplay between the two lowest multipole moments characterizing the nuclear shape, namely the quadrupole and octupole degrees of freedom has been studied in Sm and Gd isotopes with neutron number  $84 \leq N \leq 92$  [53] as well as in actinide nuclei around  $N \approx 134$  [54]. Calculations have been carried out using the parameterizations D1S [55], D1M [56] and D1M\* [57] of the Gogny-EDF. Both quadrupole and octupole constraints were considered simultaneously to build the MFPEs for the considered nuclei. Those MFPEs exhibited a soft behavior along the octupole direction indicating, that dynamical beyond-mean-field effects should be taken into account. Those beyond-mean-field effects were considered via both parity projection of the intrinsic states and symmetry-conserving quadrupole-octupole configuration mixing calculations, in the spirit of the two-dimensional (2D) Generator Coordinate Method (GCM) [58]. In addition to the systematic of the correlation energies,  $1^-$  excitation energies,  $B(E1)$  and  $B(E3)$  transition probabilities, the results of Refs. [53, 54] indicate that 2D-GCM zero-point quantum fluctuations lead to a

\*Electronic address: raynerrobertorodriguez@gmail.com

<sup>†</sup>Electronic address: luis.robledo@uam.es

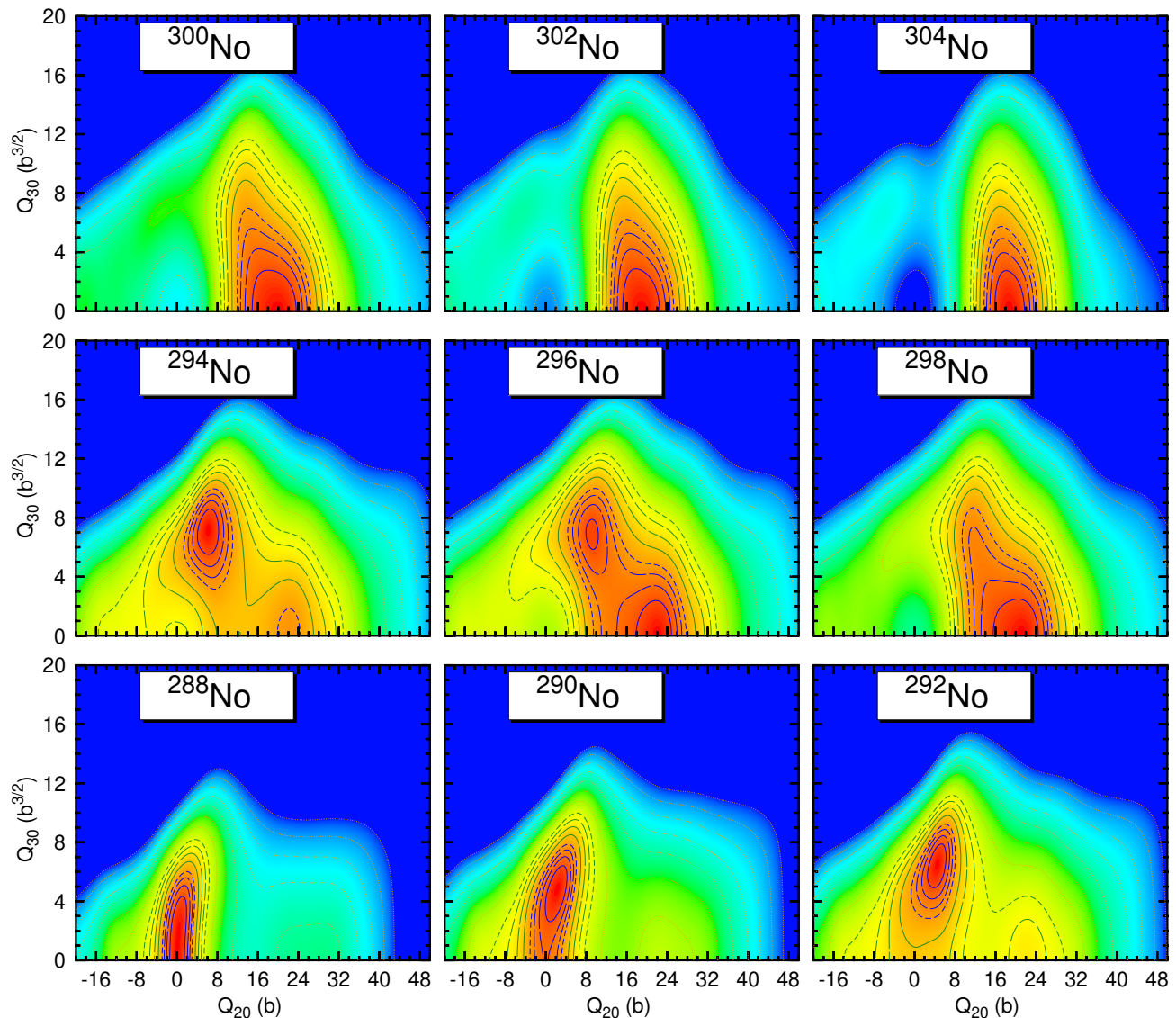


FIG. 1: (Color online) MFPEs computed with the Gogny-D1M EDF for the isotopes  $^{288-304}\text{No}$ . Dark blue contour lines extend from 0.25 MeV up to 1 MeV above the ground state energy in steps of 0.25 MeV in the ascending sequence full, long-dashed, medium-dashed and short-dashed. Dark green contour lines extend 1.5 MeV up to 3 MeV above the ground state in steps of 0.5 MeV with the same sequence of full, long-dashed, medium-dashed and short-dashed as before. From there on orange dotted contour lines are drawn in steps of 1 MeV. The color code spans a range of 10 MeV with red corresponding to the lowest energy and blue corresponding to an energy 10 MeV above. The intrinsic HFB energies are symmetric under the exchange  $Q_{30} \rightarrow -Q_{30}$ . For  $A = 294$  a quadruple deformation  $Q_{20} = 10\text{b}$  is equivalent to  $\beta_2 = 0.141$  and an octupole deformation  $Q_{30} = 1\text{b}^{3/2}$  is equivalent to  $\beta_3 = 0.021$ . For more details, see the main text.

dynamically enhanced octupolarity in the studied nuclei. The 2D-GCM framework has also been applied to Rn, Ra and Th nuclei in Ref. [59].

Octupole correlations in neutron-rich heavy and super-heavy nuclei have been the subject of intense scrutiny in recent years [22, 47–49, 60–63]. Those nuclei will not be accessible with future Radioactive Beam Facilities (RBF). However, they represent the territories where the fate of the nucleosynthesis of heavy nuclei is determined and therefore a better understanding of their properties is required, for example, to improve the modeling of fis-

sion recycling in neutron star mergers [64, 65].

Among the calculations mentioned in the previous paragraph those based on the NL3\*, DD-ME2, DD-PC1 and PC-PK1 relativistic EDFs [47, 48], have predicted an island of octupole-deformed nuclei in their ground state centered at ( $Z \approx 96$ ,  $N \approx 196$ ). An island of octupolarity has also been found with the SLy6 and SV-min zero range Skyrme-EDFs but this time centered at ( $Z \approx 100$ ,  $N \approx 190$ ) [60]. An inter-model comparison between the NL3\*, DD-ME2, DD-PC1 and PC-PK1 covariant EDFs and the UNEDF0, UNEDF1, UNEDF2, SLy4 and SV-

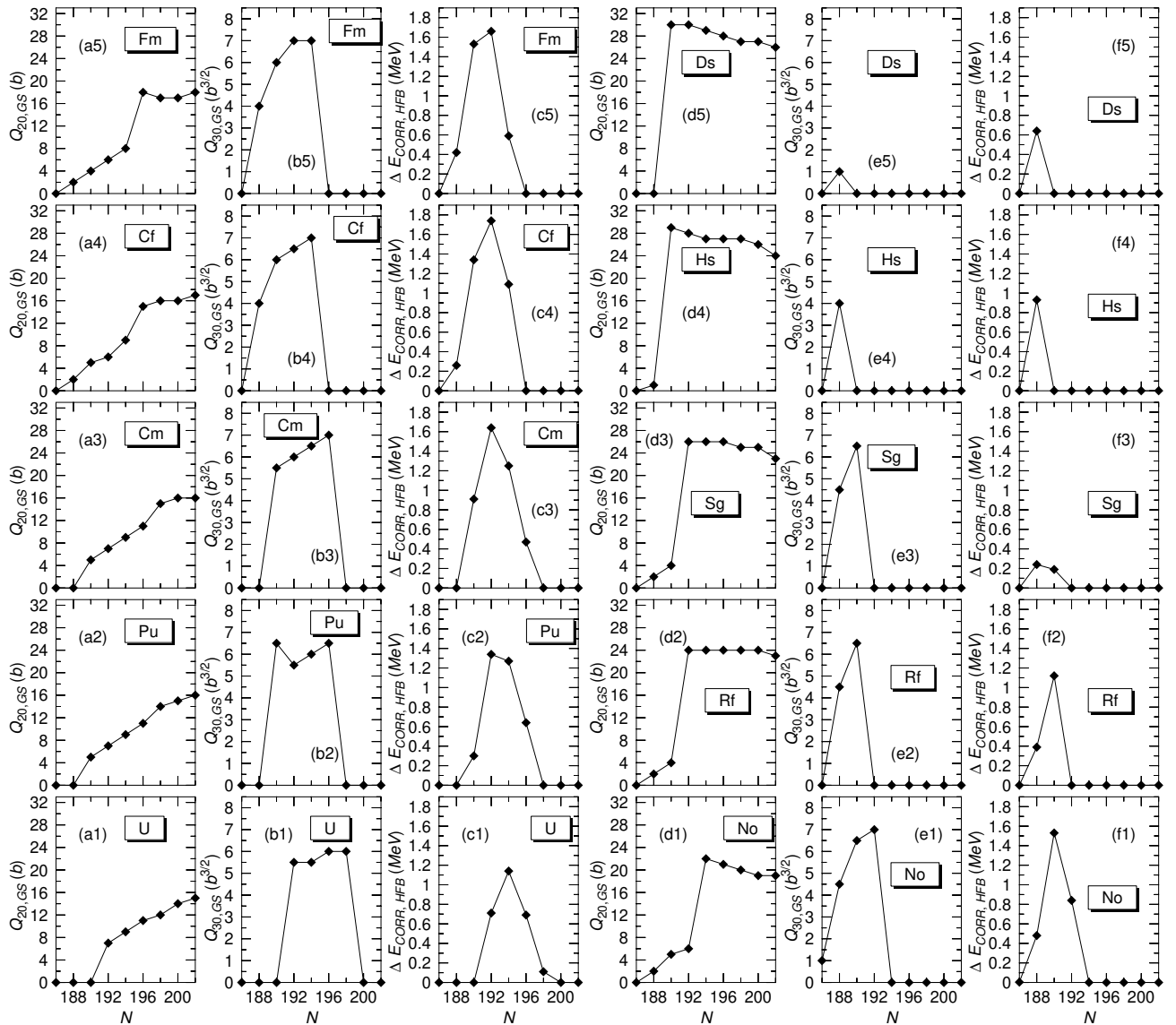


FIG. 2: The mean-field ground state quadrupole [panels (a1)-(a5) and (d1)-(d5)] and octupole [panels (b1)-(b5) and (e1)-(e5)] deformations as well as the octupole correlation energies  $\Delta E_{CORR,HFB}$  [panels (c1)-(c5) and (f1)-(f5)] Eq. (4) are plotted, as functions of the neutron number, for the nuclei  $^{278-294}\text{U}$ ,  $^{280-296}\text{Pu}$ ,  $^{282-298}\text{Cm}$ ,  $^{284-300}\text{Cf}$ ,  $^{288-302}\text{Fm}$ ,  $^{290-306}\text{Rf}$ ,  $^{292-308}\text{Sg}$ ,  $^{294-310}\text{Hs}$  and  $^{296-312}\text{Ds}$ . Results have been obtained with the Gogny-D1M EDF.

min Skyrme-EDFs have been presented in Ref. [49] for  $Z \leq 110$  and  $N \leq 210$ . It has been concluded that a region of octupole deformed ground state exists for  $184 < N < 206$ . Furthermore, calculations within the MM framework predicted an island of octupole deformation centered at  $(Z \approx 100, N \approx 184)$  [22]. Recent MM large scale calculations for  $98 \leq Z \leq 126$  and  $134 \leq N \leq 192$  predicted octupole-deformed ground states for  $N \geq 182$  [61]. Additionally, an account of the fission properties of superheavy nuclei with  $100 \leq Z \leq 126$  including very neutron-rich isotopes up to around 4 MeV from the two-neutron driplines, has predicted octupole instability for  $186 \leq N \leq 194$  using the Gogny-D1M\* EDF [62]. All the aforementioned approaches agree on the existence of an

island of octupolarity in neutron-rich actinides and low- $Z$  (i.e.,  $Z \leq 110$ ) superheavy nuclei, in spite of the differences regarding its location and extension in the  $(Z,N)$ -plane. However, the predictions of different approaches differ for larger  $Z$  values [22, 48, 60–63].

Given the relevance of dynamical octupole correlations and/or symmetry restoration in the properties associated to the octupole degree of freedom pointed out in our previous studies discussed above we have decided to apply those techniques to the region of the nuclear chart including actinides and low- $Z$  superheavies. In this work, we study the quadrupole-octupole coupling in neutron-rich even-even nuclei with proton and neutron numbers  $92 \leq Z \leq 110$  and  $186 \leq N \leq 202$ . As in previous studies cover-

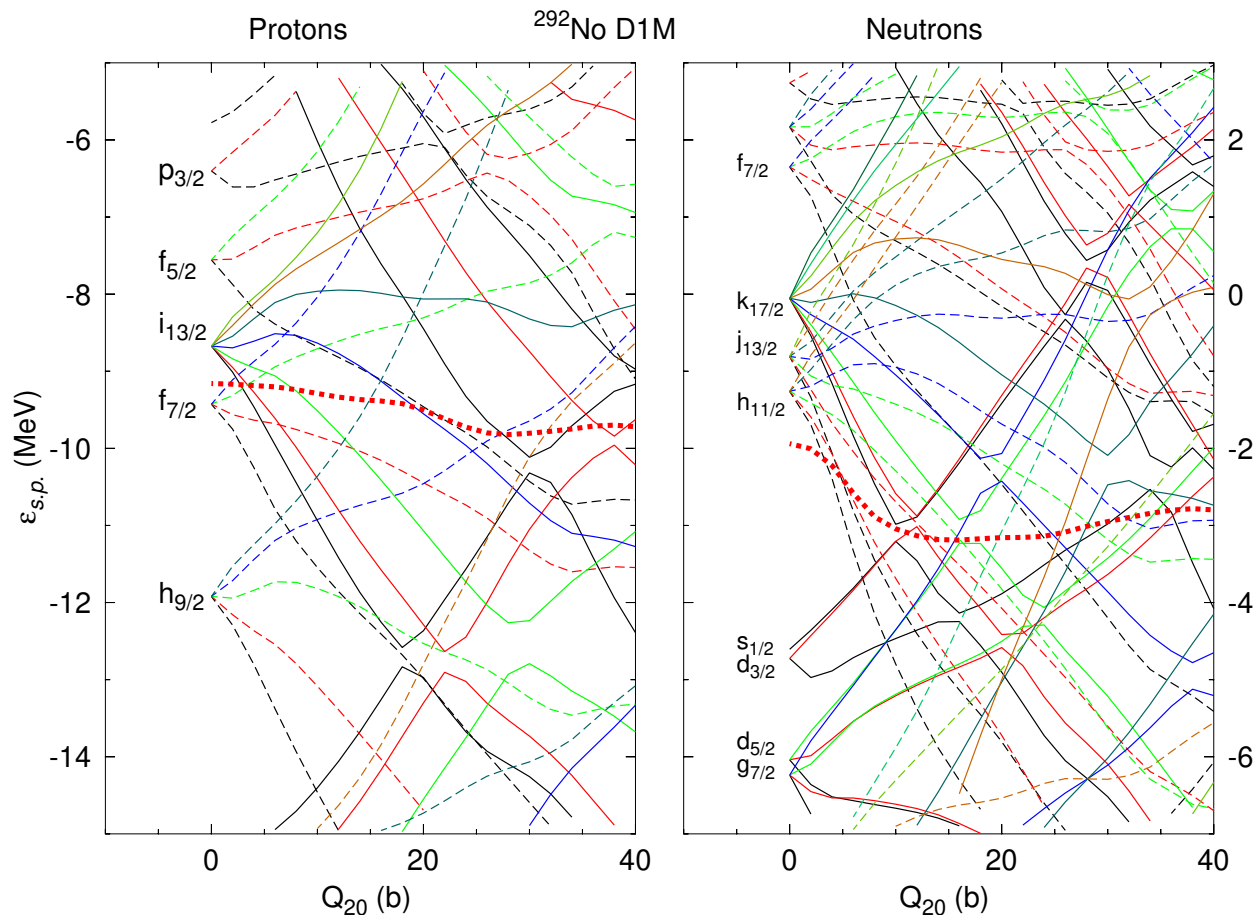


FIG. 3: (Color online) Single particle energies for protons (left panel) and neutrons (right panel) as a function of the quadrupole moment and for reflection symmetric  $Q_{30} = 0$  shapes. The spherical quantum numbers at  $Q_{20}$  are also indicated in the plot. The color code is associated with the  $K$  value of the orbital (black,  $K = 1/2$ ; red,  $K = 3/2$ ; green  $K = 5/2$ ; blue  $K = 7/2$ ; forest green  $K = 9/2$ ; brown  $K = 11/2$ , etc.). Positive (negative) parity orbitals are plotted as full (dashed) curves. The Fermi level is represented with a thick dotted red line.

ing other regions of the nuclear chart [53, 54], we consider three levels of approximation for each nucleus. First, the constrained Hartree-Fock-Bogoliubov (HFB) approach is used to obtain a set of mean field HFB wave functions, which are labeled by their intrinsic quadrupole and octupole moments. The energy associated with those HFB states is used to build a mean field potential energy surface (MFPEs) which is a function of both the quadrupole and octupole moments. As discussed later on, those MFPEs often are rather soft along the octupole direction. Some of the studied neutron-rich nuclei display a pronounced competition, i.e., shape coexistence, between reflection-symmetric and reflection-asymmetric configurations. Moreover, in some cases the MFPEs exhibits a transitional behavior along the quadrupole direction. Therefore, the HFB approximation can only be considered as a starting point and dynamical correlations stemming from the restoration of the broken parity symmetry (second level) and/or fluctuations in the collective quadrupole and octupole coordinates (third level) have to be taken into account.

The results discussed in this paper have been obtained with the finite range and density dependent Gogny-D1M EDF. Such a parametrization, specially tailored to better describe nuclear masses, has already provided a reasonable description of octupole properties [44, 50, 53, 54, 59]. However, in order to illustrate the robustness of the 2D-GCM predictions with respect to the underlying Gogny-EDF, we will also discuss results obtained with the D1S, D1M\* and D1M\*\* parametrizations for a selected set of nuclei. The parametrization D1S has been thoroughly tested all over the nuclear chart both at the mean-field level and beyond (see, for example, Ref. [66] and references therein). On the other hand, D1M\* and D1M\*\* are newly proposed re-parametrizations of D1M with the goal of improving the slope of the symmetry energy while preserving as much as possible other properties of D1M. Details of their fitting protocol can be found in Refs. [57, 67].

The paper is organized as follows. The three levels of approximation employed in this study are briefly outlined in Secs. II A and II B. In order to facilitate the discussion,

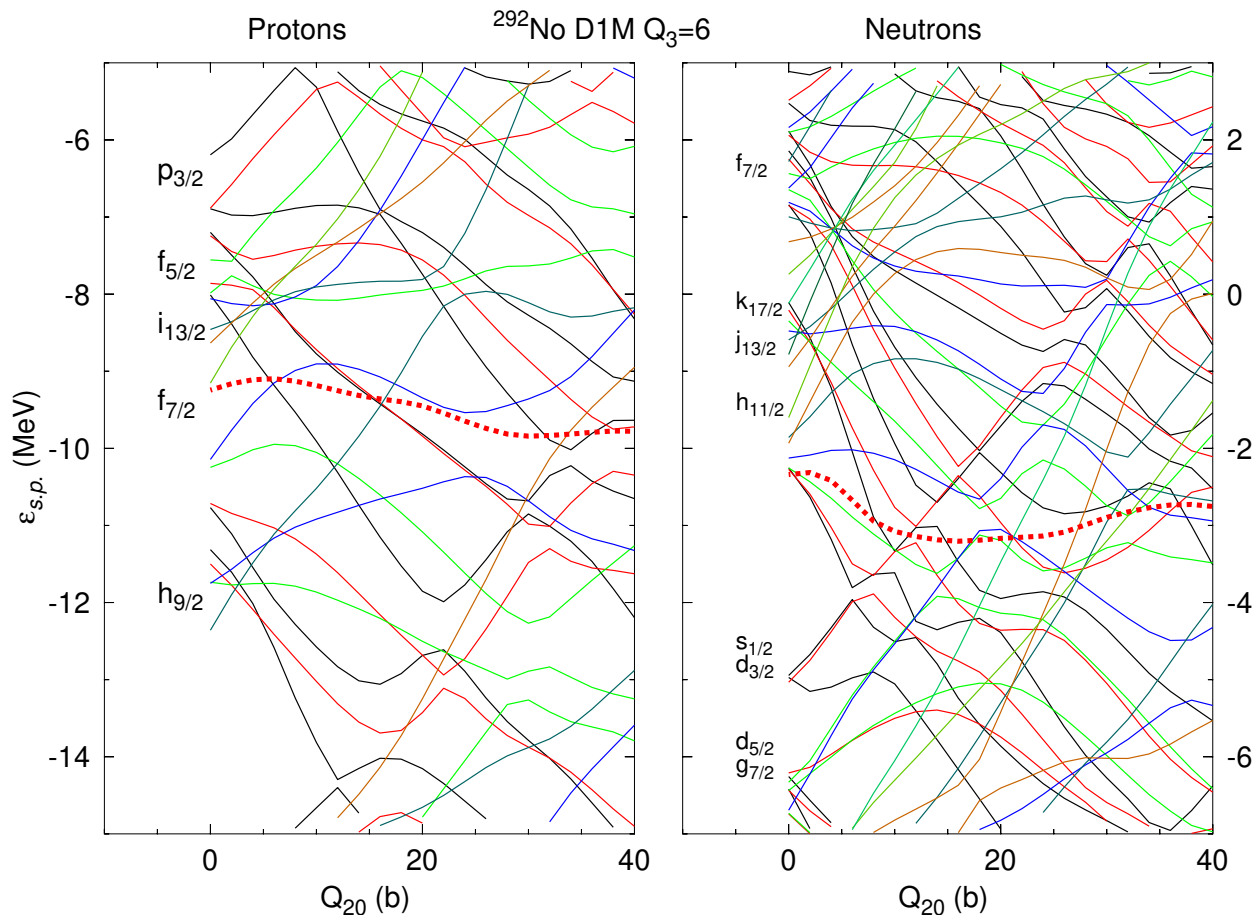


FIG. 4: (Color online) Same as Fig 3 but for reflection asymmetric shapes corresponding to  $Q_{30} = 6b^{3/2}$ . In this case, the single particle orbitals do not have a definite parity and therefore all of them are plotted with full lines.

the results obtained with the corresponding approach will be discussed in each section. The HFB results will be discussed in Sec. II A while beyond-mean-field correlations are considered in Sec. II B. First, parity-projected potential energy surfaces (PPPESs) are computed via parity projection of the intrinsic HFB states in Sec. II B 1. This level of approximation is useful to disentangle the relative contribution of parity projection to the total correlation. Second, both parity projection and fluctuations in the collective coordinates are considered via 2D-GCM calculations in Sec. II B 2. Special attention is paid in Sec. II B 2 to the systematic of  $1^-$  energy splittings, correlation energies as well as  $B(E1)$  and  $B(E3)$  transition probabilities in the considered nuclei. Furthermore, in this section, we will discuss the robustness of the 2D-GCM predictions with respect to the considered Gogny-EDF. Finally, Sec. III is devoted to the concluding remarks.

## II. RESULTS

The aim of this work is to study the quadrupole-octupole coupling in the neutron-rich nuclei  $^{278-294}\text{U}$ ,  $^{280-296}\text{Pu}$ ,  $^{282-298}\text{Cm}$ ,  $^{284-300}\text{Cf}$ ,  $^{286-302}\text{Fm}$ ,  $^{288-304}\text{No}$ ,  $^{290-306}\text{Rf}$ ,  $^{292-308}\text{Sg}$ ,  $^{294-310}\text{Hs}$  and  $^{296-312}\text{Ds}$ . Three levels of approximation have been employed: The HFB [58] scheme with constraints on the (axially symmetric) quadrupole and octupole operators, parity projection of the intrinsic state and the symmetry-conserving 2D-GCM. In what follows, we briefly outline those approaches, which were used in the past in different regions of the nuclear chart [53, 54, 59]. The different results obtained at each level of approximation will be presented and discussed.

### A. Mean-field

For each of the studied nuclei, we first build the MF-PES, i.e., the mean-field energy  $E_{HFB}(\mathbf{Q})$  as a function of the  $K = 0$  multipole deformation moments  $\mathbf{Q} = (Q_{20}, Q_{30})$ . To this end, the HFB equation with

constrains on the axially symmetric quadrupole

$$\hat{Q}_{20} = z^2 - \frac{1}{2}(x^2 + y^2) \quad (1)$$

and octupole operator

$$\hat{Q}_{30} = z^3 - \frac{3}{2}(x^2 + y^2)z \quad (2)$$

is solved using an approximate second-order gradient method [68] that guarantees a fast and reliable convergence of the selfconsistent HFB procedure. The quadrupole  $Q_{20}$  and octupole  $Q_{30}$  deformation parameters are defined via the mean values of the operators  $\hat{Q}_{20}$  and  $\hat{Q}_{30}$  in the corresponding HFB states. From the deformations  $Q_{20}$  and  $Q_{30}$ , one can easily compute [39] the deformations parameters  $\beta_2$  and  $\beta_3$  as

$$\beta_l = \frac{\sqrt{4\pi(2l+1)}}{3R_0^l A} Q_{l0} \quad (3)$$

with  $R_0 = 1.2A^{1/3}$  and  $A$  the mass number. For example, for  $A = 294$  a quadrupole deformation  $Q_{20} = 10b$  is equivalent to  $\beta_2 = 0.141$  and an octupole deformation  $Q_{30} = 1b^{3/2}$  is equivalent to  $\beta_3 = 0.021$ .

In order to alleviate the already substantial computational effort, both axial and time-reversal symmetries have been kept as self-consistent symmetries. Aside from the usual mean-field constrains on the proton and neutron numbers, the center of mass is fixed at the origin to avoid spurious effects associated with its motion [44, 53, 54, 59]. To grant convergence for the studied physical quantities the HFB quasiparticle operators ( $\hat{\alpha}_k^\dagger, \hat{\alpha}_k$ ) [58] have been expanded in a (deformed) axially symmetric harmonic oscillator (HO) basis ( $\hat{c}_l^\dagger, \hat{c}_l$ ) containing 17 major shells.

The MFPEs obtained for the isotopes  $^{288-304}\text{No}$  are shown in Fig. 1 as illustrative examples. In our calculations, the  $Q_{20}$ -grid  $-20b \leq Q_{20} \leq 50b$  (with a step  $\delta Q_{20} = 1b$ ) and the  $Q_{30}$ -grid  $0b^{3/2} \leq Q_{30} \leq 20b^{3/2}$  (with a step  $\delta Q_{30} = 0.5b^{3/2}$ ) have been employed. Along the  $Q_{20}$ -direction there is a shape/phase transition from a spherical ground state in  $^{288}\text{No}$  to well quadrupole-deformed ground states in heavier isotopes. For  $^{290-294}\text{No}$ , the MFPEs exhibit a transitional behavior along the  $Q_{20}$ -direction. Similar results are obtained for other isotopic chains. As can be seen from panels (a1)-(a5) and (d1)-(d5) of Fig. 2, the ground state quadrupole deformations  $Q_{20,GS}$  are within the range  $0b \leq Q_{20,GS} \leq 30b$ .

The MFPEs show octupole deformed minima in some No isotopes with the minima occurring always at small quadrupole deformations. A typical example is  $^{290}\text{No}$  which is octupole deformed and almost spherical. When the isotopes of No acquire a larger quadrupole deformation the octupole deformed minimum vanishes and the ground state becomes reflection symmetric with a rather soft MFPEs along the  $Q_{30}$ -direction. This pattern repeats in all the other isotopes considered in this

work as can be deduced from Fig. 2. We observe there that octupole-deformed HFB ground states are found in  $^{284-290}\text{U}$ ,  $^{284-290}\text{Pu}$ ,  $^{286-292}\text{Cm}$ ,  $^{286-292}\text{Cf}$ ,  $^{288-294}\text{Fm}$ ,  $^{288-294}\text{No}$ ,  $^{292,294}\text{Rf}$ ,  $^{294,296}\text{Sg}$ ,  $^{296}\text{Hs}$  and  $^{298}\text{Ds}$  with  $1b^{3/2} \leq Q_{30,GS} \leq 7b^{3/2}$  [see, panels (b1)-(b5) and (e1)-(e5) of Fig. 2]. These results indicate that, as in previous studies [22, 47-49, 60, 61], an island of octupole-deformed neutron-rich actinides and low-Z superheavy nuclei is found in our HFB calculations based on the the Gogny-D1M EDF. Similar results, not shown here, have also been obtained with the D1S, D1M\* and D1M\*\* parametrizations.

The HFB energy gained by breaking reflection symmetry in the ground state, defined as

$$\Delta E_{CORR,HFB} = E_{HFB,Q_{30}=0} - E_{HFB,GS} \quad (4)$$

is plotted in panels (c1)-(c5) and (f1)-(f5) of Fig. 2. The largest values of  $\Delta E_{CORR,HFB}$  correspond to  $N = 194$  (U),  $N=192$  (Pu, Cm, Cf and Fm),  $N = 190$  (No and Rf) and  $N = 188$  (Sg, Hs and Ds). The maximum value of 1.8 MeV corresponds to  $^{290}\text{Cf}$ . The relatively small  $\Delta E_{CORR,HFB}$  energies reflect the softness along the  $Q_{30}$ -direction in the MFPEs of nuclei with an octupole-deformed HFB ground state.

For some No isotopes, the MFPEs (see, Fig. 1) exhibit a pronounced competition, i.e., shape coexistence, between reflection-symmetric and reflection-asymmetric minima. For example, in the case of  $^{296}\text{No}$  the energy difference between the global reflection-symmetric  $(Q_{20,GS}, Q_{30,GS}) = (22b, 0)$  and local reflection-asymmetric  $(Q_{20}, Q_{30}) = (10b, 7b^{3/2})$  minima amounts to just 210 keV. Such a shape coexistence is also observed in other isotopic chains.

Before concluding this section, we turn our attention to single-particle properties. As it is well known, atomic nuclei "avoid" regions with high single-particle level densities (Jahn-Teller effect) and therefore the plots of single-particle energies (SPEs) as a function of quadrupole or octupole moment help us to identify regions where energy gaps (i.e. low level density regions) favor the appearance of deformed minima. For this purpose we have chosen to plot the eigenvalues of the Routhian  $h = t + \Gamma - \lambda_{Q_{20}}Q_{20} - \lambda_{Q_{30}}Q_{30}$ , where  $t$  is the kinetic energy and  $\Gamma$  the Hartree-Fock field. The term  $\lambda_{Q_{20}}Q_{20} + \lambda_{Q_{30}}Q_{30}$  contains the Lagrange multipliers used to enforce the corresponding quadrupole and octupole constrains. The single-particle energies obtained in the  $^{292}\text{No}$  case are plotted in Figs. 3 and 4, for protons and neutrons separately, as functions of the quadrupole moment. The plot of Fig. 3 corresponds to zero octupole deformation, therefore the parity of each single-particle orbital is identified with the use of full (positive parity) and dashed (negative parity) lines. On the other hand, Fig. 4 corresponds to the same kind of plot but in this case we have taken an octupole deformation  $Q_{30} = 6b^{3/2}$  that roughly corresponds with the position of the octupole deformed minima. In the later, parity is



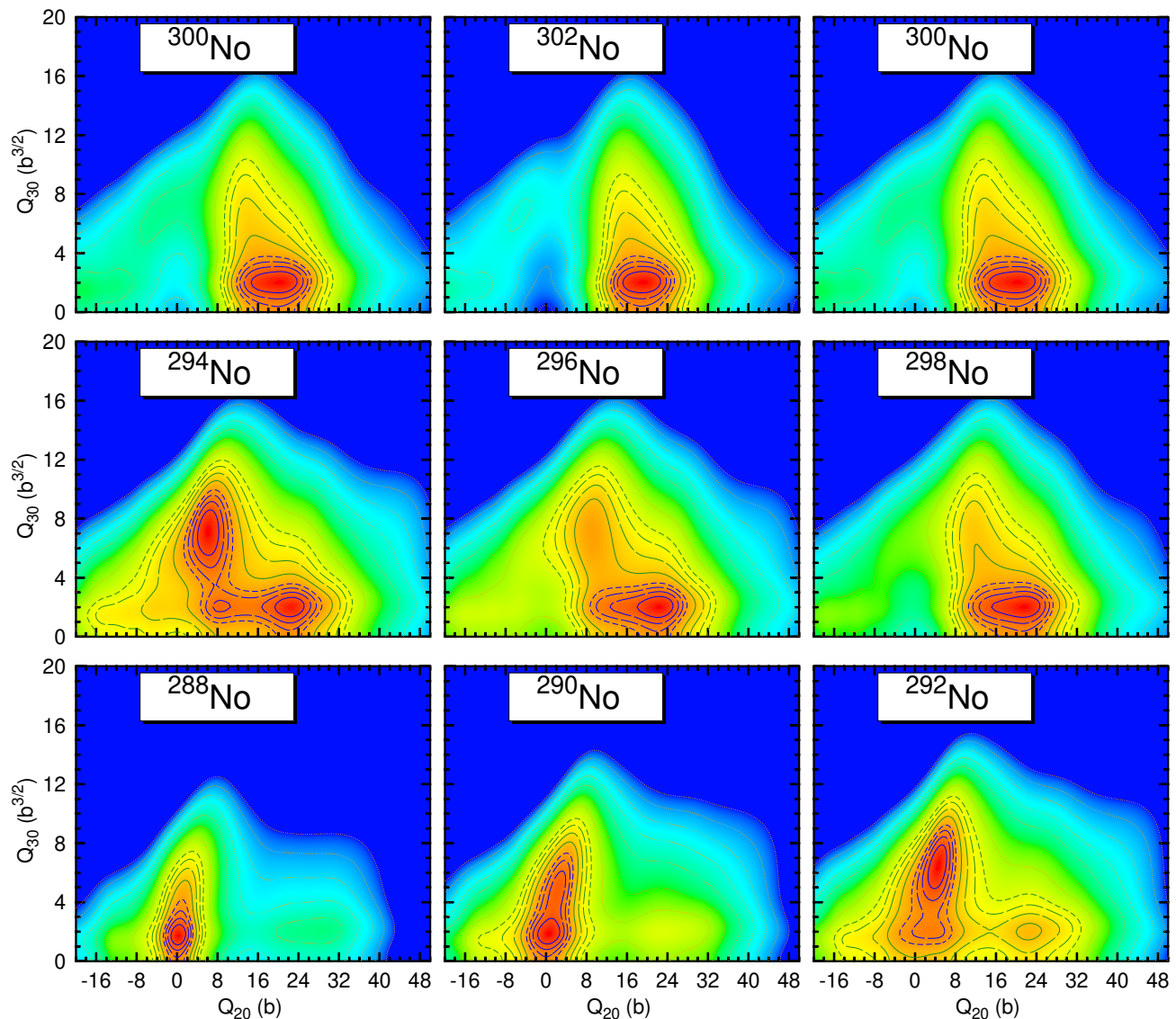


FIG. 5: (Color online) Positive parity ( $\pi = +1$ ) PPFESs computed with the Gogny-D1M EDF for the isotopes  $^{288-304}\text{No}$ . See, caption of Fig. 1 for the contour-line patterns and color scale.

not a good quantum number. Finally, the corresponding Fermi levels are plotted with a thick dotted red line. The first thing we notice in Fig. 3 is the presence of  $\Delta j = \Delta l = 3$  orbitals around the Fermi level both for protons ( $i_{13/2} - f_{7/2}$ ) and neutrons ( $k_{17/2} - h_{11/2}$ ). The presence of these opposite parity  $\Delta J = \Delta l = 3$  pairs of orbitals is a natural requirement for the existence of octupole-deformed minima. For protons and neutrons there are gaps in the spectra at the spherical configuration relatively close to the Fermi level: those gaps are the precursors of the near spherical octupole-deformed minima observed for neutron numbers  $N=186-192$ . The deformed minima observed for larger  $N$  values at  $Q_{20} \approx 18$  b are due to gaps opening up at that deformation. In Fig. 4 we depict the same type of plot but for  $Q_{30} = 6b^{3/2}$ . At  $Q_{20} = 0$  we have included the labels of the spherical orbitals at the same place where they are located in the

$Q_{30} = 0$  plot to show the strong impact of parity mixing. We observe how large shell gaps open up at  $Q_{20} = 0$  as a consequence of parity mixing that are responsible for the near spherical octupole-deformed minima obtained for  $N=186-192$ . On the other hand, for  $Q_{20} \approx 18$  b there are no clear gaps in the spectrum in agreement with the fact that there are no octupole-deformed minima for that value of the quadrupole moment.

### B. Beyond-mean-field correlations

As discussed in the previous section, the softness of the MFPEs along the octupole direction as well as the existence in some cases of coexisting minima point towards the key role of dynamical beyond-mean-field correlations, i.e., symmetry restoration and/or quadrupole-

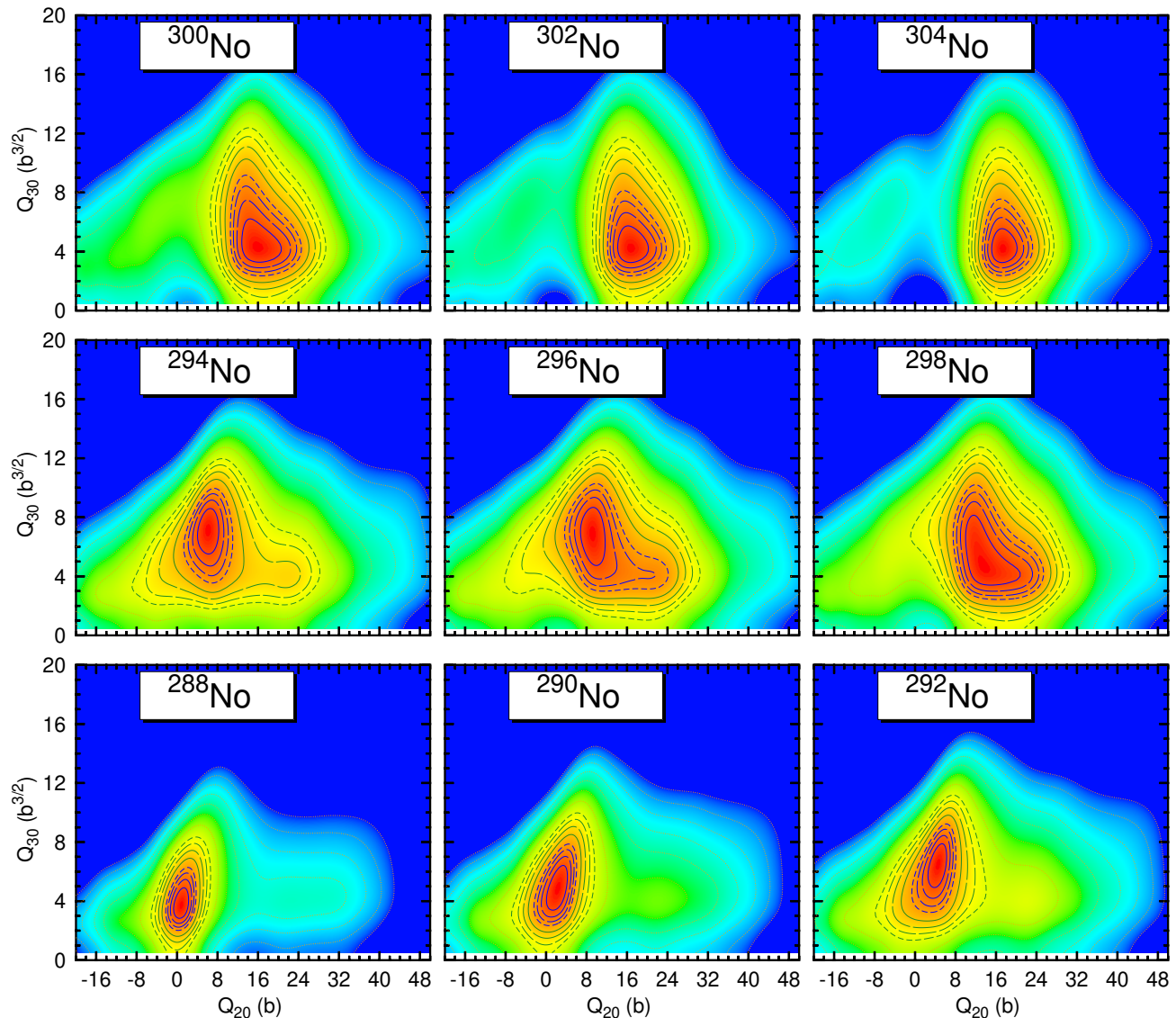


FIG. 6: (Color online) Negative parity ( $\pi = -1$ ) PPPESs computed with the Gogny-D1M EDF for the isotopes  $^{288-304}\text{No}$ . See, caption of Fig. 1 for the contour-line patterns and color scale.

octupole configuration mixing in the properties of the ground state and collective negative parity states in the studied nuclei. Since the octupole is the softest mode, the spatial reflection symmetry is the most important invariance to be restored. It would be desirable to restore also both the rotational and particle number symmetries. However, such a gigantic task is out of the scope of an exhaustive survey like the one discussed in this paper for several technical reasons (for example, the large number of HO shells used and the number of degrees of freedom required in the GCM ansatz).

### 1. Parity symmetry restoration

In order to restore the spatial reflection symmetry broken by the HFB states  $|\Phi(\mathbf{Q})\rangle$  with non-zero octupole

deformation, we resort to parity projection, i.e., we build the parity-conserving states  $|\Phi^\pi(\mathbf{Q})\rangle = \hat{\mathcal{P}}^\pi|\Phi(\mathbf{Q})\rangle$  by applying on the intrinsic state the parity projector

$$\hat{\mathcal{P}}^\pi = \frac{1}{2} (1 + \pi \hat{\Pi}), \quad (5)$$

where  $\pi = \pm 1$  is the desired parity quantum number. The energies  $E_\pi(\mathbf{Q})$ , associated with the states  $|\Phi^\pi(\mathbf{Q})\rangle$ ,



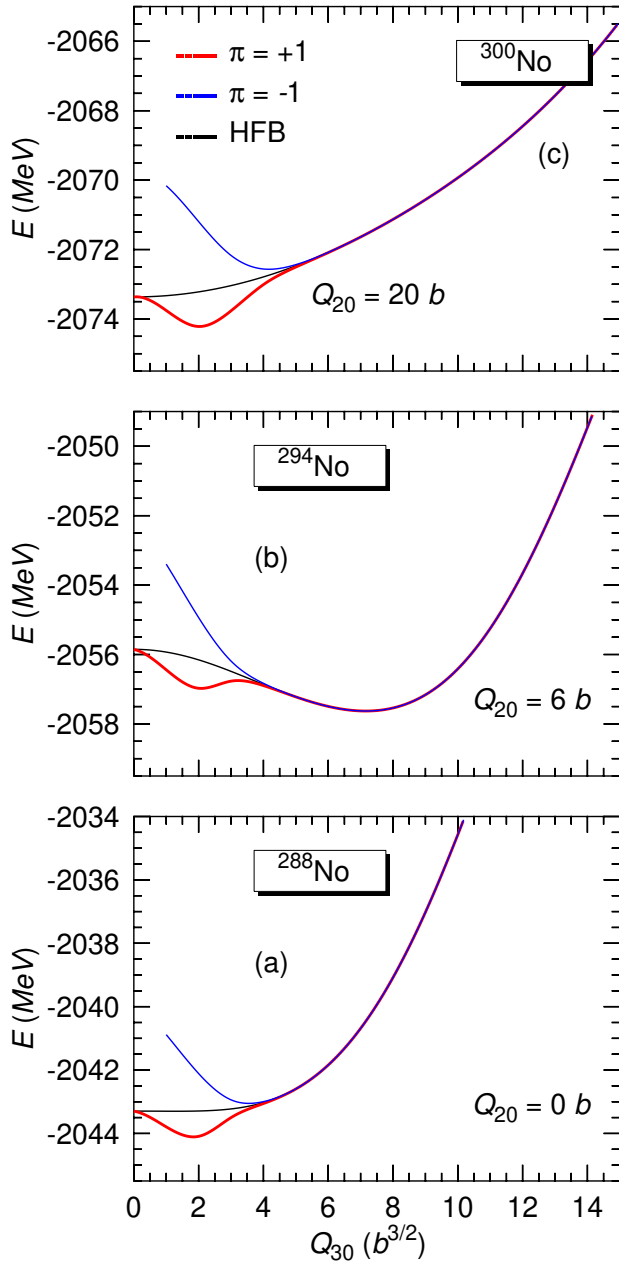


FIG. 7: (Color online) The  $\pi = +1$  (red) and  $\pi = -1$  (blue) parity-projected energies are depicted as functions of the octupole moment  $Q_{30}$  for fixed values of the quadrupole moment  $Q_{20}$  in the nuclei  $^{288}\text{No}$ ,  $^{294}\text{No}$  and  $^{300}\text{No}$ . The corresponding HFB energies are also included in the plots. Results have been obtained with the Gogny-D1M EDF.

define the PPPEs. They read

$$\begin{aligned}
 E_{\pi}(\mathbf{Q}) = & \frac{\langle \Phi(\mathbf{Q}) | \hat{H}[\rho(\vec{r})] | \Phi(\mathbf{Q}) \rangle}{2 \langle \Phi(\mathbf{Q}) | \hat{\mathcal{P}}^{\pi} | \Phi(\mathbf{Q}) \rangle} \\
 & + \pi \frac{\langle \Phi(\mathbf{Q}) | \hat{H}[\theta(\vec{r})] \hat{\Pi} | \Phi(\mathbf{Q}) \rangle}{2 \langle \Phi(\mathbf{Q}) | \hat{\mathcal{P}}^{\pi} | \Phi(\mathbf{Q}) \rangle} \\
 & - \lambda_Z \left( \frac{\langle \Phi(\mathbf{Q}) | \hat{Z} \hat{\mathcal{P}}^{\pi} | \Phi(\mathbf{Q}) \rangle}{\langle \Phi(\mathbf{Q}) | \hat{\mathcal{P}}^{\pi} | \Phi(\mathbf{Q}) \rangle} - Z_0 \right) \\
 & - \lambda_N \left( \frac{\langle \Phi(\mathbf{Q}) | \hat{N} \hat{\mathcal{P}}^{\pi} | \Phi(\mathbf{Q}) \rangle}{\langle \Phi(\mathbf{Q}) | \hat{\mathcal{P}}^{\pi} | \Phi(\mathbf{Q}) \rangle} - N_0 \right). \quad (6)
 \end{aligned}$$

Because the Gogny force used is a density dependent one we need a prescription for the density dependent contribution to the energy overlaps. As in previous studies [53, 54, 59] we use the density

$$\rho(\vec{r}) = \frac{\langle \Phi(\mathbf{Q}) | \hat{\rho}(\vec{r}) | \Phi(\mathbf{Q}) \rangle}{\langle \Phi(\mathbf{Q}) | \Phi(\mathbf{Q}) \rangle} \quad (7)$$

to compute  $\langle \Phi(\mathbf{Q}) | \hat{H}[\rho(\vec{r})] | \Phi(\mathbf{Q}) \rangle$  and the density

$$\theta(\vec{r}) = \frac{\langle \Phi(\mathbf{Q}) | \hat{\rho}(\vec{r}) \hat{\Pi} | \Phi(\mathbf{Q}) \rangle}{\langle \Phi(\mathbf{Q}) | \hat{\Pi} | \Phi(\mathbf{Q}) \rangle} \quad (8)$$

in the evaluation of  $\langle \Phi(\mathbf{Q}) | \hat{H}[\theta(\vec{r})] \hat{\Pi} | \Phi(\mathbf{Q}) \rangle$ . In this way we avoid the pathologies found in the restoration of spatial symmetries [69–72]. As the parity-projected proton and neutron numbers, usually differ from the nucleus' proton  $Z_0$  and neutron  $N_0$  numbers, we have introduced first-order corrections in Eq. (6), with  $\lambda_Z$  and  $\lambda_N$  being chemical potentials for protons and neutrons, respectively [53, 54, 59, 73, 74].

The  $\pi = +1$  and  $\pi = -1$  PPPEs obtained for the isotopes  $^{288-304}\text{No}$  are depicted in Figs. 5 and 6 as illustrative examples. Since  $\hat{\Pi}|\Phi(Q_{20}, Q_{30} = 0)\rangle = |\Phi(Q_{20}, Q_{30} = 0)\rangle$ , the projection onto positive parity is unnecessary for those states. On the other hand, in the case of negative parity, the evaluation of the projected energy along the  $Q_{30} = 0$  axis requires to resolve 0/0 indeterminacy [36] and therefore it is subject to numerical inaccuracies [53, 54]. However, the negative parity projected energy  $E_{\pi=-1}(\mathbf{Q})$  Eq. (6) increases rapidly when approaching  $Q_{30} = 0$  (see, Fig. 7) [53, 54] and its limiting value [36] is high enough as not to play a significant role in the discussion of the  $\pi = -1$  PPPEs. We have then omitted this quantity along the  $Q_{30} = 0$  axis in Fig. 6. It is worth to notice that the quadrupole moments corresponding to the absolute minima of the  $\pi = +1$  and  $\pi = -1$  PPPEs are close to the HFB values.

As can be seen from Figs. 1, 5 and 7, not only the MFPEs but also the  $\pi = +1$  PPPEs are rather soft along the  $Q_{30}$ -direction. In the case of nuclei with small and/or zero HFB ground state octupole deformations, such as  $^{288}\text{No}$  and  $^{300}\text{No}$ , the  $\pi = +1$  PPPEs only display an absolute minimum around  $Q_{30} = 2.0b^{3/2}$ . This is illustrated in panels (a) and (c) of Fig. 7 where the

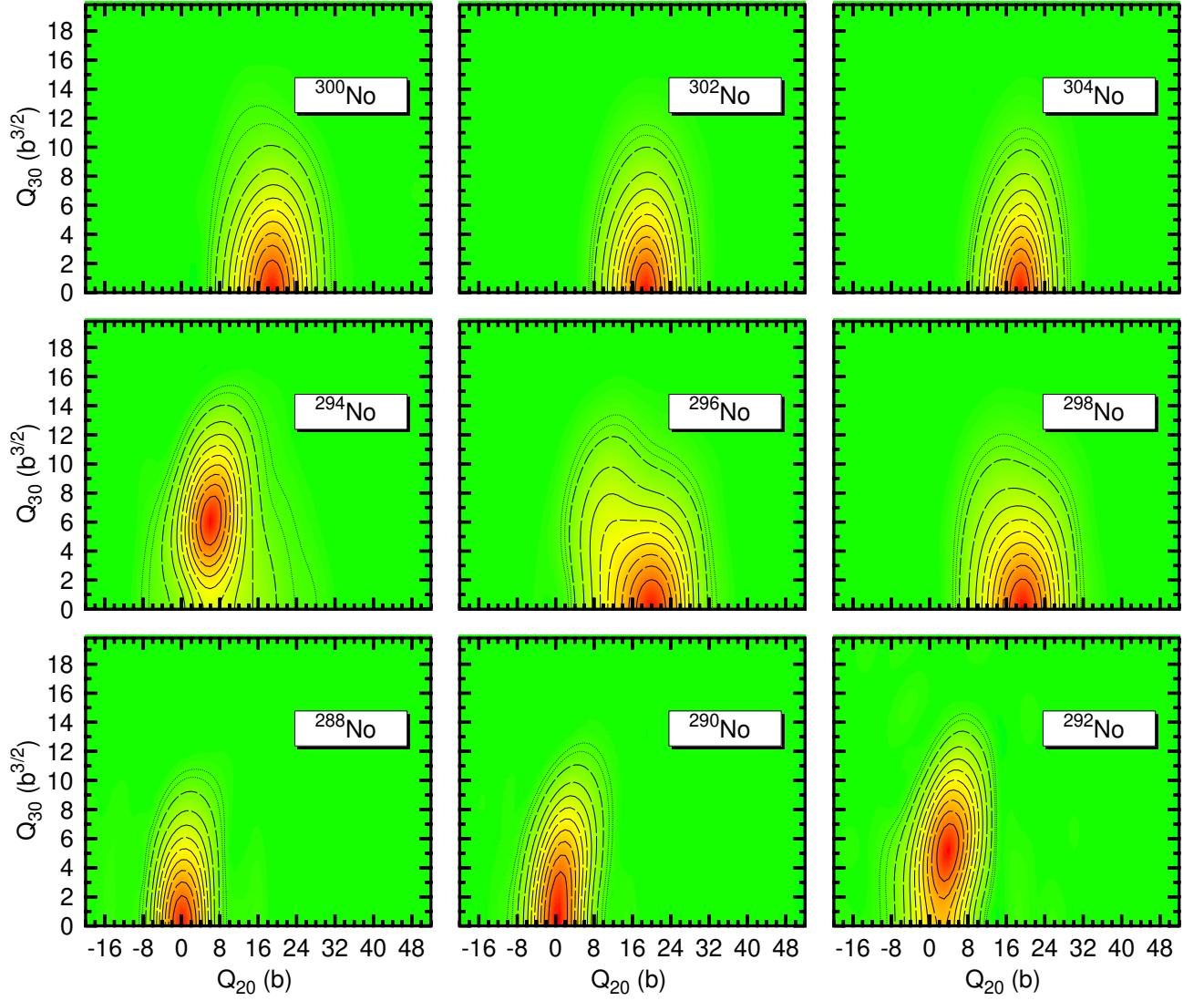


FIG. 8: Collective wave functions Eq. (14) for the ground states of the nuclei  $^{288-304}\text{No}$ . The contour lines (a succession of solid, long dashed and short dashed lines) start at 90% of the maximum value up to 10% of it. The two dotted-line contours correspond to the tail of the amplitude (5% and 1% of the maximum value). The color scale ranges from red (maximum value) to green (zero). Results have been obtained with the Gogny-D1M EDF. For more details, see the main text.

$\pi = +1$  parity-projected energies obtained for  $^{288}\text{No}$  and  $^{300}\text{No}$  are plotted, as functions of  $Q_{30}$ , for a fixed value of the quadrupole moment corresponding to the absolute minimum of the PES. However, the topography along the  $Q_{30}$ -direction is more complex for nuclei with larger HFB octupole deformations as the  $\pi = +1$  PPPEs exhibit a pronounced competition between two minima. In the case of  $^{294}\text{No}$ , for example, the energy difference between the local  $Q_{30} = 2.0b^{3/2}$  and global  $Q_{30} = 7.0b^{3/2}$  minima [see, panel (b) of Fig. 7] amounts to 652 keV. Note also from panel (b) of Fig. 7, the energy degeneracy of the absolute HFB and  $\pi = +1$  minima in this case. Furthermore, as can be seen from Fig. 5, for  $^{294}\text{No}$  the shape coexistence extends to a third minimum, located at  $(Q_{20}, Q_{30}) = (22b, 2b^{3/2})$ , which is only 14 keV above the absolute one.

The  $\pi = -1$  PPPEs, depicted in 6, exhibit in all the cases a well developed absolute minimum. In the case of nuclei such as  $^{288}\text{No}$  and  $^{300}\text{No}$ , the absolute  $\pi = -1$  minimum corresponds to a larger octupole deformation than the  $\pi = +1$  one [see, panels (a) and (c) of Fig. 7]. On the other hand, for  $^{294}\text{No}$ , the (degenerate)  $\pi = -1$  and  $\pi = +1$  absolute minima have similar octupole deformations [see, panel (b) of Fig. 7]. Similar features have been found for other isotopic chains. Let us mention, that the complex topography found for the PPPEs along the  $Q_{30}$ -direction in our Gogny-D1M calculations has already been studied, as a function of the strength of the two-body interaction, using parity-projection on the Lipkin-Meshkov-Glick (LMG) model [75].

As a measure of the correlations induced by parity pro-

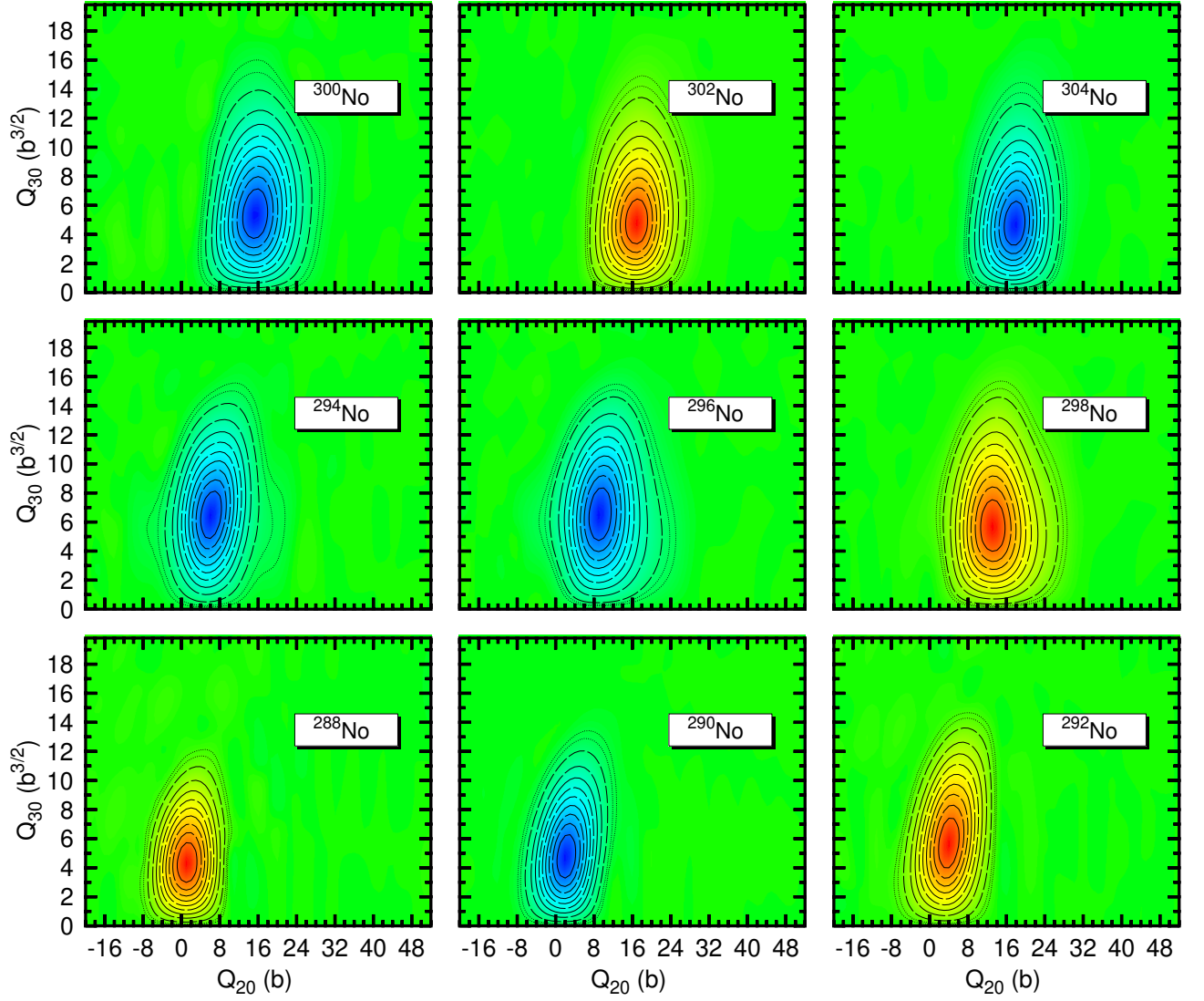


FIG. 9: (Color online) Collective wave functions Eq. (14) for the lowest negative-parity states of the nuclei  $^{288-304}\text{No}$ . See, caption of Fig. 8 for contour-line patterns. Results have been obtained with the Gogny-D1M EDF. For more details, see the main text.

jection, we consider the correlation energy

$$\Delta E_{CORR,PP} = E_{HFB,GS} - E_{\pi=+1,GS}. \quad (9)$$

defined in terms of the difference between the HFB  $E_{HFB,GS}$  and parity-projected  $E_{\pi=+1,GS}$  ground state energies. In Fig. 10, we show this quantity for the studied nuclei. The correlation energy  $\Delta E_{CORR,PP}$  is zero or nearly zero for U, Pu, Cm, Cf, Fm and No isotopes with  $190 \leq N \leq 194$  as for these nuclei the  $\pi = +1$  PPPEs display features, along the  $Q_{30}$ -direction, similar to the ones discussed above for  $^{294}\text{No}$ , i.e., the HFB and  $\pi = +1$  absolute minima are degenerate or nearly degenerate. As will be discussed in Sec II B 2, the comparison between the correlation energies  $\Delta E_{CORR,PP}$  and the ones obtained within the symmetry-conserving 2D-GCM framework reveals the key role played by quantum fluctuations around those neutron numbers.

## 2. Generator Coordinate Method

The dynamical interplay between the quadrupole and octupole degrees of freedom is considered via the 2D-GCM ansatz

$$|\Psi_{\sigma}^{\pi}\rangle = \int d\mathbf{Q} f_{\sigma}^{\pi}(\mathbf{Q}) |\Phi(\mathbf{Q})\rangle \quad (10)$$

where, both positive and negative octupole moments  $Q_{30}$  are included in the integration domain to assure the parity-conserving nature of the states  $|\Psi_{\sigma}^{\pi}\rangle$  [53, 54, 59]. The index  $\sigma$  in Eq. (10) labels the different GCM solutions.

The amplitudes  $f_{\sigma}^{\pi}(\mathbf{Q})$  are solutions of the Griffin-Hill-Wheeler (GHW) equation [58]

$$\int d\mathbf{Q}' (\mathcal{H}(\mathbf{Q}, \mathbf{Q}') - E_{\sigma}^{\pi} \mathcal{N}(\mathbf{Q}, \mathbf{Q}')) f_{\sigma}^{\pi}(\mathbf{Q}') = 0 \quad (11)$$

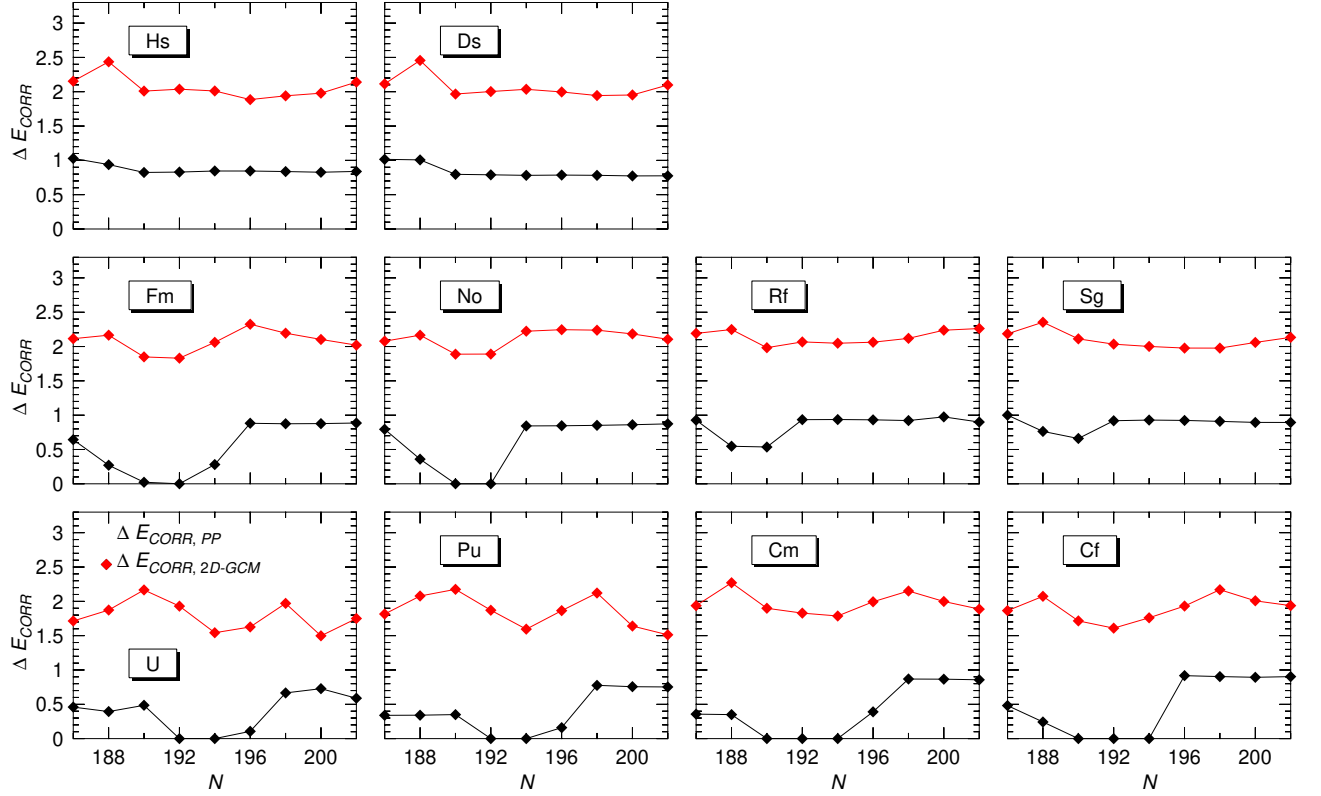


FIG. 10: (Color online) The correlation energies obtained within the 2D-GCM framework Eq. (18) are plotted as functions of the neutron number. The correlation energies  $\Delta E_{CORR,PP}$  Eq. (9) stemming from the restoration of reflection symmetry are also included in the plots. Results have been obtained with the Gogny-D1M EDF. For more details, see the main text.

with the Hamiltonian and norm kernels given by

$$\begin{aligned}
 \mathcal{H}(\mathbf{Q}, \mathbf{Q}') &= \langle \Phi(\mathbf{Q}) | \hat{H}[\rho^{GCM}(\vec{r})] | \Phi(\mathbf{Q}') \rangle \\
 &\quad - \lambda_Z \left( \langle \Phi(\mathbf{Q}) | \hat{Z} | \Phi(\mathbf{Q}') \rangle - Z_0 \mathcal{N}(\mathbf{Q}, \mathbf{Q}') \right) \\
 &\quad - \lambda_N \left( \langle \Phi(\mathbf{Q}) | \hat{N} | \Phi(\mathbf{Q}') \rangle - N_0 \mathcal{N}(\mathbf{Q}, \mathbf{Q}') \right) \\
 \mathcal{N}(\mathbf{Q}, \mathbf{Q}') &= \langle \Phi(\mathbf{Q}) | \Phi(\mathbf{Q}') \rangle.
 \end{aligned} \tag{12}$$

As in previous studies [53, 54, 59] we use the *mixed* density prescription

$$\rho^{GCM}(\vec{r}) = \frac{\langle \Phi(\mathbf{Q}) | \hat{\rho}(\vec{r}) | \Phi(\mathbf{Q}') \rangle}{\langle \Phi(\mathbf{Q}) | \Phi(\mathbf{Q}') \rangle} \tag{13}$$

in the density dependent term of the Hamiltonian kernel. As in the parity projection case Eq. (6), we use a perturbative first-order correction in the Hamiltonian kernel  $\mathcal{H}(\mathbf{Q}, \mathbf{Q}')$  to take into account deviations in both the proton and neutron numbers [53, 59, 73, 74].

The HFB basis intrinsic states  $|\Phi(\mathbf{Q})\rangle$  are not orthonormal. Therefore, the amplitudes  $f_\sigma^\pi(\mathbf{Q})$  cannot be interpreted as probability amplitudes. Instead, one considers the so-called collective wave functions

$$G_\sigma^\pi(\mathbf{Q}) = \int d\mathbf{Q}' \mathcal{N}^{\frac{1}{2}}(\mathbf{Q}, \mathbf{Q}') f_\sigma^\pi(\mathbf{Q}'), \tag{14}$$

written in terms of the operational square root of the norm kernel  $\mathcal{N}^{\frac{1}{2}}(\mathbf{Q}, \mathbf{Q}')$  [53, 54, 58, 59, 69].

The overlaps of one and two body operators between different HFB states are evaluated with the efficient pfaffian techniques of Refs [76–78].

For the reduced transition probabilities  $B(E1, 1^- \rightarrow 0^+)$  and  $B(E3, 3^- \rightarrow 0^+)$  the rotational formula for  $K=0$  bands has been used

$$B(E\lambda, \lambda^- \rightarrow 0^+) = \frac{e^2}{4\pi} \left| \langle \Psi_\sigma^{\pi=-1} | \hat{\mathcal{O}}_\lambda | \Psi_{\sigma'=1}^{\pi'=+1} \rangle \right|^2. \tag{15}$$

For  $B(E1)$  and  $B(E3)$  transitions  $\sigma$  corresponds to the first excited GCM state with negative parity. The electromagnetic transition operators  $\hat{\mathcal{O}}_1$  and  $\hat{\mathcal{O}}_3$  are the dipole moment operator and the proton component of the octupole operator, respectively [53]. The overlap  $\langle \Psi_\sigma^\pi | \hat{\mathcal{O}} | \Psi_{\sigma'}^{\pi'} \rangle$  of an operator  $\hat{\mathcal{O}}$  between two different GCM states Eq. (10) can be evaluated according to the expressions given in Refs. [53, 54].

The collective wave functions Eq. (14) corresponding to the ground and lowest negative-parity 2D-GCM states in  $^{288-304}\text{No}$  are plotted in Figs. 8 and 9, respectively. As can be seen from Fig. 8, the ground state collective amplitude  $G_{\sigma=1}^{\pi=+1}(Q_{20}, Q_{30})$  shows the typical Gaussian shape along both the quadrupole and octupole directions with a maximum located at octupole moments different from zero in  $^{292,294}\text{No}$ . The same holds for  $^{284,286}\text{U}$ ,

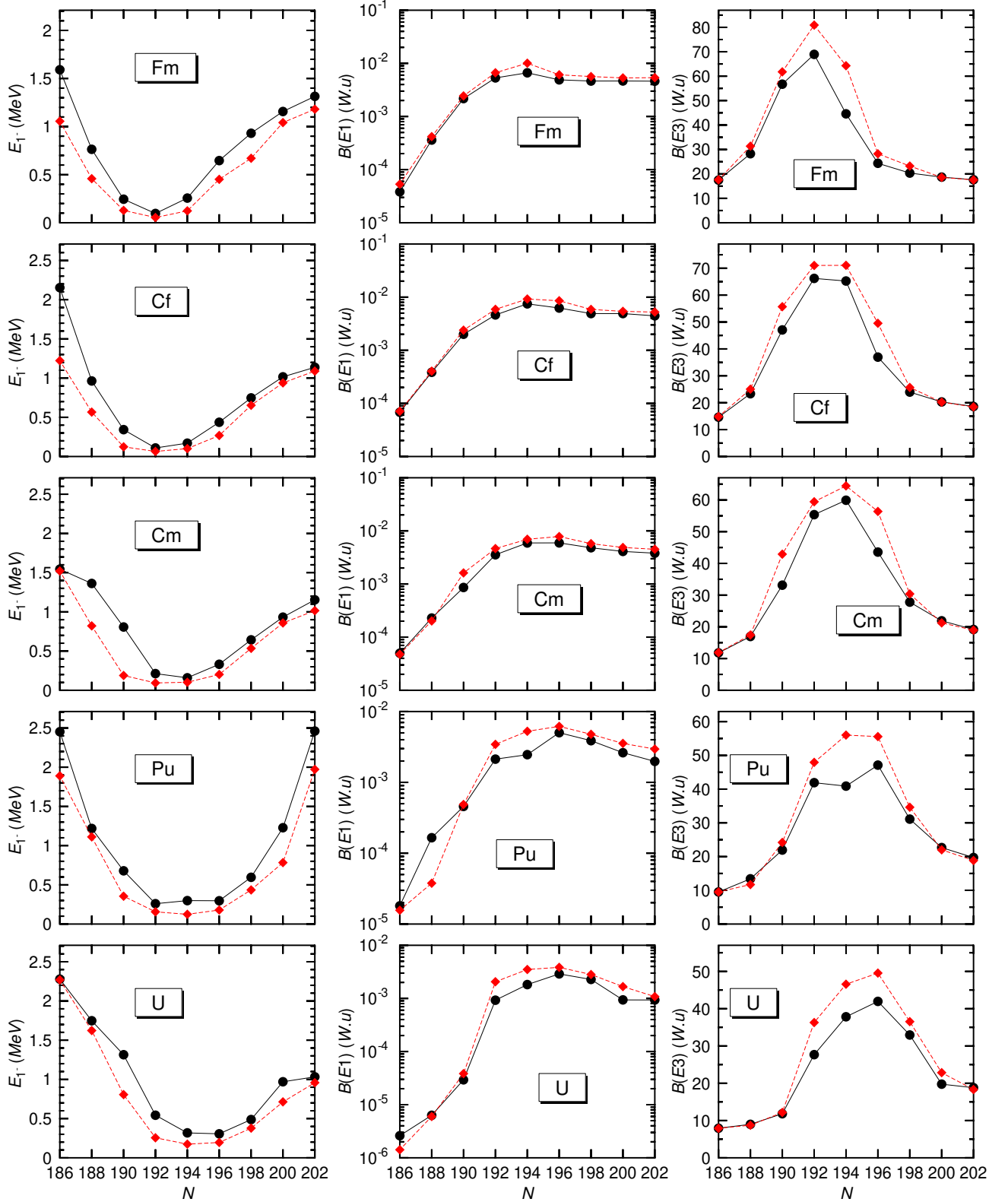


FIG. 11: (Color online) The 2D-GCM  $E_{1-}$  energy splittings (left panels) and the reduced transition probabilities  $B(E1)$  (middle panels) and  $B(E3)$  (right panels) are plotted (in black) as functions of the neutron number for the studied U, Pu, Cm, Cf and Fm isotopic chains. The  $E_{1-}$ ,  $B(E1)$  and  $B(E3)$  values obtained in the framework of the 1D-GCM, with the octupole moment as single generating coordinate, have also been included (in red) in each of the plots. Results have been obtained with the Gogny-D1M EDF. For more details, see the main text.



$^{286-290}\text{Pu}$ ,  $^{286-290}\text{Cm}$ ,  $^{288-292}\text{Cf}$ ,  $^{290,292}\text{Fm}$ ,  $^{294}\text{Rf}$  and  $^{296}\text{Sg}$ . For other nuclei the peaks of the ground state collective amplitudes are located around  $Q_{30} = 0$ . The spreading of  $G_{\sigma=1}^{\pi=+1}(Q_{20}, Q_{30})$  along the  $Q_{30}$ -direction is large, indicating the octupole-soft character of the 2D-GCM ground states obtained for the considered nuclei. On the other hand, for the negative parity amplitudes  $G_{\sigma}^{\pi=-1}(Q_{20}, Q_{30})$ , depicted in Fig. 9, the shape of the wave function is again Gaussian along the  $Q_{20}$ -direction whereas along the  $Q_{30}$ -direction it shows the characteristic shape of the first excited state of the harmonic oscillator (odd under the exchange of sign in  $Q_{30}$ ) with a zero value at  $Q_{30} = 0$  as well as a maximum and a minimum, one at a positive  $Q_{30}$  value and the other at the corresponding negative value. As a consequence, the negative parity wave function maximum or minimum always take place at a nonzero octupole moment. This is in agreement with the position of the minima of the  $\pi = -1$  PPPEs (see, Fig. 6).

The 2D-GCM average quadrupole moment is defined as

$$(\bar{Q}_{20})_{\sigma}^{\pi} = \langle \Psi_{\sigma}^{\pi} | \hat{Q}_{20} | \Psi_{\sigma}^{\pi} \rangle \quad (16)$$

and the ground state values  $(\bar{Q}_{20})_{\sigma=1}^{\pi=+1}$ , corroborate the mean field result, i.e., with increasing neutron number, for each of the studied isotopic chains, there is a transition to well quadrupole-deformed ground states. Similarly, the average quadrupole moments of the first negative parity excited state  $(\bar{Q}_{20})_{\sigma}^{\pi=-1}$ , increase with increasing neutron number.

We have also computed the average octupole moment [53, 54]

$$(\bar{Q}_{30})_{\sigma}^{\pi} = 4 \int_{\mathcal{D}} d\mathbf{Q} d\mathbf{Q}' G_{\sigma}^{\pi*}(\mathbf{Q}) \mathcal{Q}_{30}(\mathbf{Q}, \mathbf{Q}') G_{\sigma}^{\pi}(\mathbf{Q}') \quad (17)$$

and obtained, for all the studied nuclei, non zero values in the range  $0.37b^{3/2} \leq (\bar{Q}_{30})_{\sigma=1}^{\pi=+1} \leq 5.41b^{3/2}$ . At variance with the static HFB results of Sec. II A, once parity-projected quadrupole-octupole configuration mixing effects are taken into account via the 2D-GCM ansatz Eq. (10), the ground states of all the studied nuclei are (dynamically) octupole-deformed albeit with the largest octupole deformations  $(\bar{Q}_{30})_{\sigma=1}^{\pi=+1}$  corresponding to U, Pu, Cm, Cf, Fm, No, Rf and Sg isotopes with  $190 \leq N \leq 196$ . For the octupole moments  $(\bar{Q}_{30})_{\sigma}^{\pi=-1}$  we have obtained values in the range  $2.57b^{3/2} \leq (\bar{Q}_{30})_{\sigma}^{\pi=-1} \leq 6.17b^{3/2}$  and their largest values correspond once more to U, Pu, Cm, Cf, Fm, No, Rf and Sg isotopes with  $190 \leq N \leq 196$ .

The 2D-GCM correlation energy

$$\Delta E_{CORR,2D-GCM} = E_{HFB,GS} - E_{\pi=+1,2D-GCM} \quad (18)$$

is defined as the difference between the HFB and 2D-GCM ground-state energies. This quantity is plotted in Fig. 10 along with the correlation energy  $\Delta E_{CORR,PP}$  stemming from symmetry restoration alone. The comparison between both correlation energies reveals that 2D-GCM zero-point quantum fluctuations substantially

modify the behavior of  $\Delta E_{CORR,PP}$  for U, Pu, Cm, Cf, Fm and No isotopes with  $190 \leq N \leq 196$  providing a weaker dependence of  $\Delta E_{CORR,2D-GCM}$  with the neutron number. A weaker trend is also obtained for Rf and Sg nuclei around  $N=190$ . This agrees well with previous results for Sm, Gd and actinide nuclei [53, 54]. Moreover, the range of values of the correlation energy  $1.49\text{MeV} \leq \Delta E_{CORR,2D-GCM} \leq 2.45\text{MeV}$  is of the same order of magnitude as the rms for the binding energy in Gogny-like nuclear mass tables [56] and, therefore, those correlation energies should be considered in future parametrizations of the Gogny-EDF.

The 2D-GCM energy difference between the positive-parity ground state and the lowest  $1^-$  excited state is depicted in the left panels of Figs. 11 and 12 as a function of the neutron number. The  $1^-$  excitation energies are very small ( $0.10\text{MeV} \leq E_{1^-} \leq 0.36\text{MeV}$ ) for U, Pu, Cm, Cf, Fm, No, Rf and Sg isotopes with  $190 \leq N \leq 196$  in agreement with their large dynamical octupole deformations. Note, that in the case of Hs and Ds isotopes, the  $E_{1^-}$  values obtained for  $^{298}\text{Hs}$  (0.60 MeV) and  $^{298}\text{Ds}$  (0.93 MeV) are slightly larger than the previous ones. Other nuclei, with less pronounced dynamical octupole deformation effects, exhibit larger  $E_{1^-}$  values pointing towards the octupole vibrational character of their first negative-parity excited state. In the same panels, we have also included the  $E_{1^-}$  energies obtained within 1D-GCM calculations with  $Q_{30}$  as single generating coordinate. It is satisfying to observe that both calculations predict very similar trends with neutron number though the 2D-GCM energies are larger than the 1D-GCM ones.

The  $B(E1)$  transition probabilities are plotted in the middle panels of Figs. 11 and 12. For  $92 \leq Z \leq 102$ , they exhibit a steady increase up to  $N=192$  while for larger neutron numbers, the  $B(E1)$  strengths remain almost constant. Exception made of  $^{298,300}\text{Ds}$ , a steady increase is also observed for  $Z \geq 104$  up to  $N=190$ . At variance with the results obtained for lower- $Z$  chains, exception made of  $^{296}\text{Rf}$  and  $^{298,300}\text{Sg}$ , the  $B(E1)$  values also increase for larger neutron numbers, being the effect more pronounced in the Hs and Ds isotopic chains. Note, that the behavior of the  $B(E1)$  strengths with neutron number is not correlated with the behavior of the negative parity excitation energies and the  $B(E3)$  strengths (discussed below). Therefore, it is not strictly correlated with the amount of octupole correlations. This is a consequence of the strong dependence of the dipole moment with orbital occupancies [35] that leads, for instance, to strong suppression of the  $E1$  strength in some specific nuclei [39, 79] and not in their neighbors. As can be seen from the figures, the  $B(E1)$  transition probabilities obtained within 1D-GCM calculations exhibit the same pattern with neutron number as the 2D-GCM ones.

The  $B(E3)$  transition probabilities are plotted in the right panels of Figs. 11 and 12. Contrary to the  $B(E1)$  case, the magnitude of the  $B(E3)$  strength is strongly correlated with the excitation energy of the collective negative parity state, i.e., whenever this excitation energy

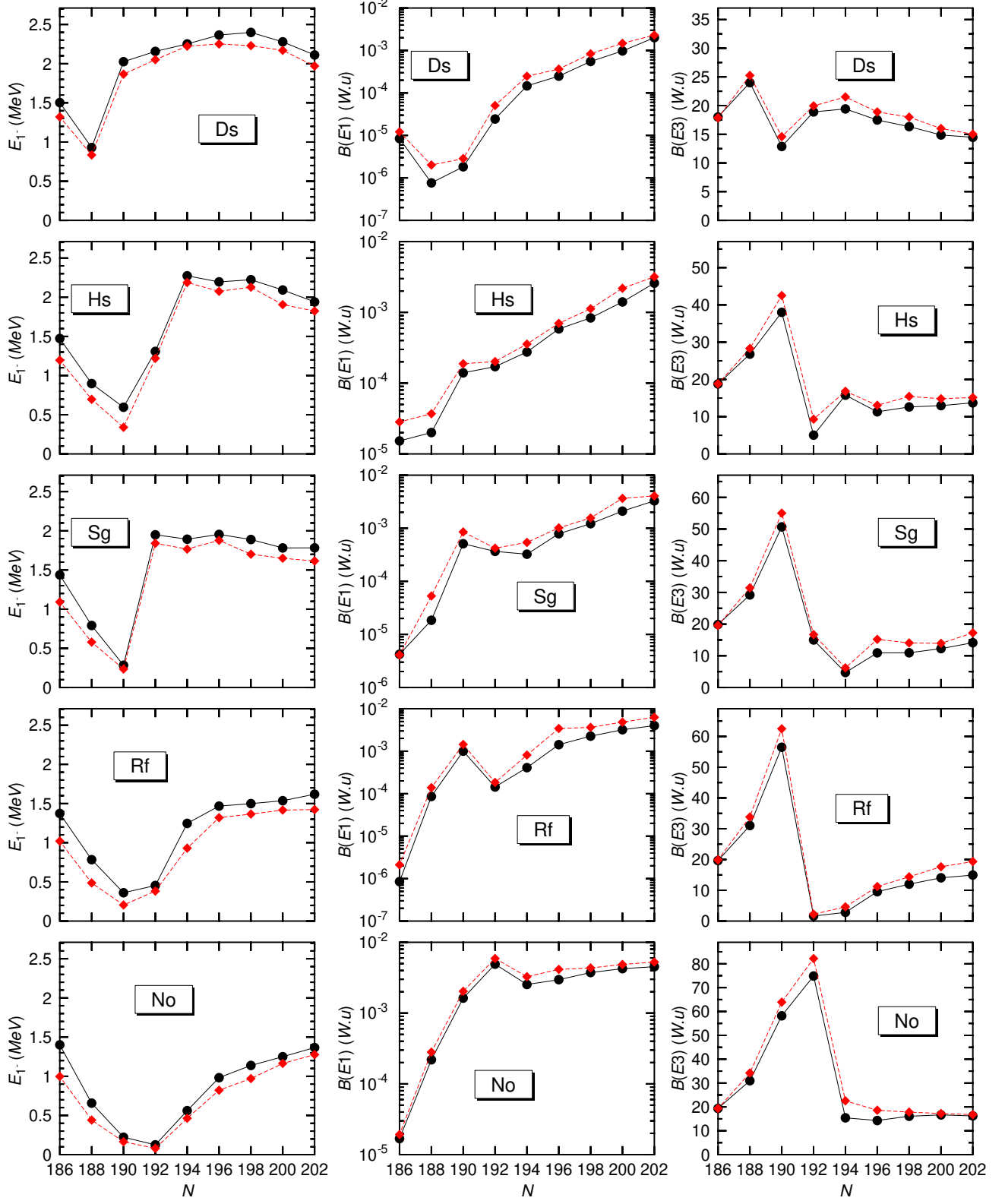


FIG. 12: (Color online) The same as Fig. 11 but for the No, Rf, Sg, Hs and Ds isotopic chains.

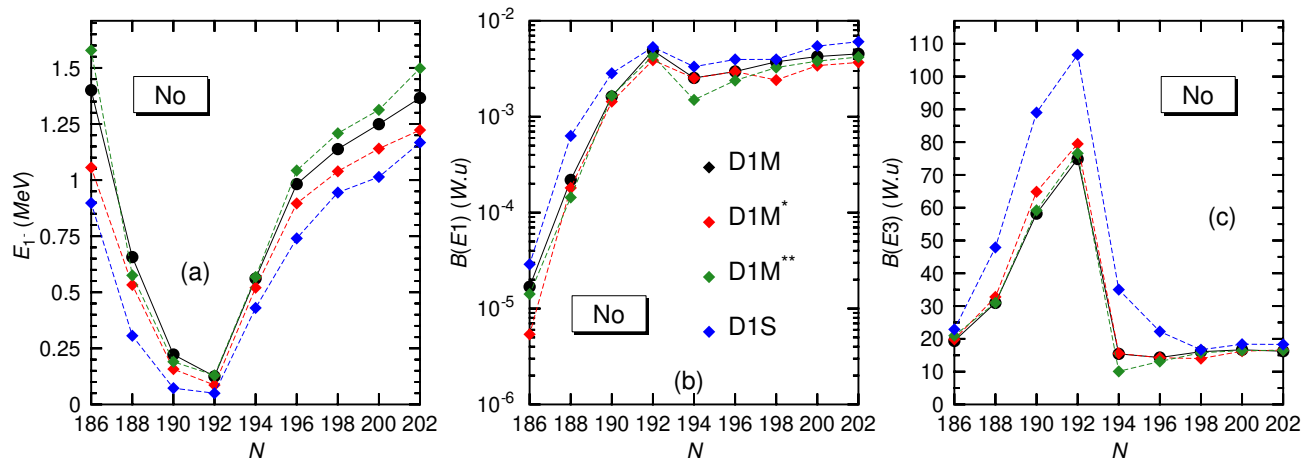


FIG. 13: (Color online) The 2D-GCM  $E_{1-}$  energy splittings [panel (a)] and the reduced transition probabilities  $B(E1)$  [panel (b)] and  $B(E3)$  [panel (c)] are plotted as functions of the neutron number for the isotopes  $^{288-304}\text{No}$ . Results have been obtained with the parametrizations D1S, D1M, D1M\* and D1M\*\* of the Gogny-D1M EDF. For more details, see the main text.

is small the  $B(E3)$  strength is large. Exception made of  $^{296}\text{No}$  and  $^{298}\text{Rf}$ , this correspondence is obeyed in all the considered nuclei. The MFPEs obtained for  $^{296}\text{No}$  (see Fig. 1) and  $^{298}\text{Rf}$ , exhibit a pronounced competition between two minima at almost the same energy but with quite different  $Q_{20}$  and  $Q_{30}$  deformations. This shape coexistence leads to a rather low excitation energy of the  $1^-$  state. However, the collective wave functions for the ground and negative parity states barely overlap, leading to a reduction in the  $B(E3)$  value. For other nuclei, the ground state collective wave function is peaked at a non-zero octupole deformation and therefore strongly overlaps with the one of the negative parity state (see, Figs. 8 and 9) leading to a large  $B(E3)$  value. For less octupole correlated systems, the peak of the ground state collective wave function shifts to  $Q_{30} = 0$  and therefore the overlap with the negative parity collective wave function is severely reduced as it is the  $E3$  strength. As can be seen from the figures, the 1D-GCM and 2D-GCM  $B(E3)$  transition probabilities display the same trend with the most pronounced quantitative differences being obtained for U, Pu, Cm, Cf and Fm isotopes around  $N = 194$ .

In the comparison between 1D-GCM and 2D-GCM calculations, one should keep in mind that even when the corresponding collective wave functions look similar along the octupole direction, their tiny differences can be associated with the differences in the results. The comparison between 1D-GCM and 2D-GCM results in Figs. 11 and 12 reveals that, to a large extent, there is a decoupling between the quadrupole and octupole degrees of freedom in the studied nuclei and indicates that the 1D-GCM framework represents a valuable computational tool to account for the systematics of the  $1^-$  excitation energies and transition probabilities in this exotic region of the nuclear chart.

Finally, in order to illustrate the robustness of the 2D-GCM predictions with respect to the underlying Gogny-

EDF, calculations have also been carried out with the parametrizations D1S, D1M\* and D1M\*\* for  $^{288-304}\text{No}$ . The results are depicted in Fig. 13. The largest quantitative differences are obtained with the D1S parametrization, as expected, because D1M\* and D1M\*\* were fitted to be as close as possible to D1M. However, from the comparison we conclude that the predicted trends, with neutron number, of the  $1^-$  excitation energies and reduced transition probabilities are rather insensitive to the Gogny-EDF employed in the calculations.

### III. CONCLUSIONS

In this paper we have studied the interplay between quadrupole and octupole degrees of freedom in a set of even-even neutron-rich actinides and superheavy nuclei with  $92 \leq Z \leq 110$  and  $186 \leq N \leq 202$  both at the mean-field level and beyond. To this end, we have resorted to the Gogny-HFB framework, parity projection and 2D-GCM configuration mixing calculations with the quadrupole  $Q_{20}$  and octupole  $Q_{30}$  moments as generating coordinates.

Static octupole deformations are found around the "octupole neutron magic number"  $N=192$  in roughly 30 % of the 90 nuclei analyzed. On the other hand, dynamical octupole deformations are ubiquitous and have a significant impact on correlation energies leading to a weaker dependence with neutron number. The consideration of beyond-mean-field effects within the 2D-GCM approach allows us to explore properties of the lowest-lying collective negative parity excited states such as, their excitation energies and transition strengths to the positive parity ground state. Low excitation energies and large  $E3$  strengths are observed in nuclei with strong octupole correlations. The  $E1$  strength, as expected, is a less collective quantity and does not show a clear correlation

with octupole properties.

Given that very neutron-rich isotopes are considered, a comparison with experimental data is not possible at present and probably will not be possible in the future. However, the properties analyzed can be used to model the nuclear reactions taking place in the r-process nucleosynthesis of superheavy nuclei. The relevance of this lies on the fact that the population of short lived superheavy nuclei is thought to have an impact on the solar abundance of mid-mass elements in the rare earth region through fission recycling.

## Acknowledgments

The work of LMR was supported by Spanish Ministry of Economy and Competitiveness (MINECO) Grants No. PGC2018-094583-B-I00. We acknowledge the computer resources and assistance provided by Centro de Computación Científica-Universidad Autónoma de Madrid (CCC-UAM).

- 
- [1] P.A. Butler and W. Nazarewicz, *Rev. Mod. Phys.* **68**, 349 (1996).
- [2] R. Rodríguez-Guzmán and L. M. Robledo, *Phys. Rev. C* **89**, 054310 (2014).
- [3] R. Rodríguez-Guzmán and L. M. Robledo, *Eur. Phys. J. A* **53**, 245 (2017).
- [4] N. Schunck and L. M. Robledo, *Rep. Prog. Phys.* **79**, 116301 (2016).
- [5] M. Warda and L. M. Robledo, *Phys. Rev. C* **84**, 044608 (2011).
- [6] I. Ahmad and P. A. Butler, *Ann. Rev. Nucl. Part. Sci.* **43**, 71 (1993).
- [7] P. A. Butler, *J. Phys. G* **43**, 073002 (2016).
- [8] P. A. Butler and L. Willmann, *Nucl. Phys. News* **25**, 12 (2015).
- [9] S. K. Tandel, M. Hemalatha, A. Y. Deo, S. B. Patel, R. Palit, T. Trivedi, J. Sethi, S. Saha, D. C. Biswas and S. Mukhopadhyay, *Phys. Rev. C* **87**, 034319 (2013).
- [10] H. J. Li, S. J. Zhu, J. H. Hamilton, E. H. Wang, A. V. Ramayya, Y. J. Chen, J. K. Hwang, J. Ranger, S. H. Liu, Z. G. Xiao, Y. Huang, Z. Zhang, Y. X. Luo, J. O. Rasmussen, I. Y. Lee, G. M. Ter-Akopian, Y. T. Oganessian and W. C. Ma, *Phys. Rev. C* **90**, 047303 (2014).
- [11] I. Ahmad, R. R. Chasman, J. P. Greene, F. G. Kondev and S. Zhu, *Phys. Rev. C* **92**, 024313 (2015).
- [12] B. Bucher, S. Zhu, C.Y. Wu, R.V.F. Janssens, D. Cline, A.B. Hayes, *et al.*, *Phys. Rev. Lett.* **116**, 112503 (2016).
- [13] B. Bucher, S. Zhu, C.Y. Wu, R.V.F. Janssens, R.N. Bernard, L.M. Robledo, *et al.*, *Phys. Rev. Lett.* **118**, 152504 (2017).
- [14] P. A. Butler, L. P. Gaffney, P. Spagnoletti, K. Abrahams, M. Bowry, J. Cederkall, *et al.*, *Phys. Rev. Lett.* **124**, 042503 (2020).
- [15] L. P. Gaffney *et al.*, *Nature* **497**, 199 (2013).
- [16] M. M. R. Chishti, D. O'Donnell, *et al.*, *Nature Physics* (2020).
- [17] L. I. Schiff, *Phys. Rev. C* **132**, 2194 (1963).
- [18] J. Dobaczewski, J. Engel, M. Kortelainen and P. Becker, *Phys. Rev. Lett.* **121**, 232501 (2018).
- [19] P. Möller and J.R. Nix, *Nucl. Phys.* **A361**, 117 (1981).
- [20] A. Gyurkovich, A. Sobczewski, B. Nerlo-Pomorska and K. Pomorski, *Phys. Lett. B* **105**, 95 (1981).
- [21] W. Nazarewicz, P. Olanders, I. Ragnarsson, J. Dudek, G. Leander, P. Möller and E. Ruchowska, *Nucl. Phys.* **A429**, 269 (1984).
- [22] P. Möller, J. Nix, W. D. Meyers and W. Swiatecki, *At. Data Nucl. Data Tables* **59**, 185 (1995).
- [23] P. Möller, R. Bengtson, B. G. Carlsson, P. Olivius, T. Ichikawa, H. Sagawa and A. Iwamoto, *At. Data Nucl. Data Tables* **94**, 758 (2008).
- [24] K. Nomura, D. Vretenar, T. Niksic and Bing-Nan Lu, *Phys. Rev. C* **89**, 024312 (2014).
- [25] K. Nomura, T. Niksic and D. Vretenar, *Phys. Rev. C* **97**, 024317 (2018).
- [26] K. Nomura, D. Vretenar and B. -N. Lu, *Phys. Rev. C* **88**, 021303(R) (2013).
- [27] K. Nomura, R. Rodríguez-Guzmán and L. M. Robledo, *Phys. Rev. C* **92**, 014312 (2015).
- [28] S. Marcos, H. Flocard, and P.H. Heenen, *Nucl. Phys.* **A410**, 125 (1983).
- [29] P. Bonche, P. -H. Heenen, H. Flocard, and D. Vautherin, *Phys. Lett.* **B175**, 387 (1986).
- [30] P. Bonche, S.J. Krieger, M.S. Weiss, J. Dobaczewski, H. Flocard, and P.-H. Heenen, *Phys. Rev. Lett.* **66**, 876 (1991).
- [31] P.-H. Heenen, J. Skalski, P. Bonche, and H. Flocard, *Phys. Rev. C* **50**, 802 (1994).
- [32] J. Erler, K. Langanke, H. P. Loens, G. Martínez-Pinedo and P.-G. Reinhard, *Phys. Rev. C* **85**, 025802 (2012).
- [33] L.M. Robledo, J.L. Egido, J.F. Berger, and M. Girod, *Phys. Lett.* **B187**, 223 (1987).
- [34] L.M. Robledo, J.L. Egido, B. Nerlo-Pomorska, and K. Pomorski, *Phys. Lett.* **B201**, 409 (1988).
- [35] J.L. Egido and L.M. Robledo, *Nucl. Phys.* **A518**, 475 (1990).
- [36] J.L. Egido and L.M. Robledo, *Nucl. Phys.* **A524**, 65 (1991).
- [37] E. Garrote, J.L. Egido, and L.M. Robledo, *Phys. Rev. Lett.* **80**, 4398 (1998); *Nucl. Phys.* **A654**, 723c (1999).
- [38] L.M. Robledo, M. Baldo, P. Schuck, and X. Viñas, *Phys. Rev. C* **81**, 034315 (2010).
- [39] J.L. Egido and L.M. Robledo, *Nucl. Phys.* **A545**, 589 (1992).
- [40] W. H. Long, J. Meng, N. Van Giai and S. G. Zhou, *Phys. Rev. C* **69**, 034319 (2004).
- [41] Rémi N. Bernard, Luis M. Robledo and Tomás R. Rodríguez, *Phys. Rev. C* **93**, 061302(R) (2016).
- [42] Z. Xu and Z.-P. Li, *Chinese Phys. C* **41**, 124107 (2017).
- [43] Z. P. Li, B. Y. Song, J. M. Mao, D. Vretenar and J. Meng, *J. Phys. G: Nucl. Part. Phys.* **42**, 055109 (2015).
- [44] L. M. Robledo and R. Rodríguez-Guzmán, *J. Phys. G: Nucl. Part. Phys.* **39**, 105103 (2012).
- [45] S. Ebata and T. Nakatsukasa, *Physica Scr.* **92**, 064005 (2017).
- [46] S. Y. Xia, H. Tao, Y. Lu, Z. P. Li, T. Niksic and D.

- Vretenar, Phys. Rev. C **96**, 054303 (2017).
- [47] S. E. Agbemava, A. V. Afanasjev and P. Ring, Phys. Rev. C **93**, 044304 (2016).
- [48] S. E. Agbemava and A. V. Afanasjev, Phys. Rev. C **96**, 024301 (2017).
- [49] Y. Cao, S. E. Agbemava, A. V. Afanasjev, W. Nazarewicz and E. Olsen, arXiv:2004.01319v1 [nucl-th].
- [50] L. M. Robledo and G. F. Bertsch, Phys. Rev. C **84**, 054302 (2011).
- [51] L. M. Robledo, J. Phys. G: Nucl. Part. Phys. **42** 055109 (2015).
- [52] J. Dechargé and D. Gogny, Phys. Rev. C **21**, 1568 (1980).
- [53] R. Rodríguez-Guzmán, L. M. Robledo and P. Sarriguren, Phys. Rev. C **86**, 034336 (2012).
- [54] R. Rodríguez-Guzmán, Y.M. Humadi and L. M. Robledo, J. Phys. G: Nucl. Part. Phys. **48**, 015103 (2021).
- [55] J. F. Berger, M. Girod, and D. Gogny, Nucl. Phys. A **428**, 23c (1984).
- [56] S. Goriely, S. Hilaire, M. Girod and S. Péru, Phys. Rev. Lett. **102**, 242501 (2009).
- [57] C. Gonzalez-Boquera, M. Centelles, X. Vinas and L. M. Robledo, Phys. Lett. B **779**, 195 (2018).
- [58] P. Ring and P. Schuck, *The Nuclear Many-Body Problem* (Springer, Berlin-Heidelberg-New York) (1980).
- [59] L. M. Robledo and P. A. Butler, Phys. Rev. C **88**, 051302(R) (2013).
- [60] J. Erler, K. Langanke, H.P. Loens, G. Martínez-Pinedo and P.-G. Reinhard, Phys. Rev. C **85**, 025802 (2012).
- [61] P. Jachimowicz, M. Kowal and J. Skalski, arXiv:2010.10018v1 [nucl-th].
- [62] R. Rodríguez-Guzmán, Y. M. Humadi and L. M. Robledo, Eur. Phys. J. A, **56**, 43 (2020).
- [63] M. Warda and J.L. Egido, Phys. Rev. C **86**, 014322 (2012).
- [64] S. Goriely, A. Bauswein and H.-T. Hanka, Astr. Phys. J. **738**, L32 (2011).
- [65] O. Just, A. Bauswein, R. A. Pulpillo, S. Goriely and H.-T. Hanka, Mont. Not. R. Astr. Soc. **448**, 541 (2015).
- [66] L. M. Robledo, Tomás R. Rodríguez and R. Rodríguez-Guzmán, J. Phys. G: Nucl. Part. Phys. **46**, 013001 (2019).
- [67] X. Vinas, C. Gonzalez-Boquera, M. Centelles, C. Mondal and L. M. Robledo, Acta. Phys. Pol. **12**, 705 (2019).
- [68] L.M. Robledo and G.F. Bertsch, Phys. Rev. C **84**, 014312 (2011).
- [69] R. R. Rodríguez-Guzmán, J. L. Egido, and L.M. Robledo, Nucl. Phys. **A709**, 201 (2002).
- [70] J.L. Egido and L.M. Robledo, Lecture Notes in Physics **641**, 269 (2004).
- [71] L. M. Robledo, Int. J. of Mod. Phys. E **16**, 337 (2007).
- [72] L. M. Robledo, J. Phys. G: Nucl. Part. Phys. **37**, 064020 (2010).
- [73] K. Hara, A. Hayashi and P. Ring, Nucl. Phys. **A385**, 14 (1982).
- [74] P. Bonche, J. Dobaczewski, H. Flocard, P.-H. Heenen and J. Meyer, Nucl. Phys. **A510**, 466 (1990).
- [75] L. M. Robledo, Phys. Rev. C **46**, 238 (1992).
- [76] L. M. Robledo, Phys. Rev. C **79**, 021302(R) (2009).
- [77] L. M. Robledo, Phys. Rev. C **84**, 014307 (2011).
- [78] G. F. Bertsch and L. M. Robledo, Phys. Rev. Lett. **108**, 042505 (2012)
- [79] J.L. Egido and L.M. Robledo, Nucl. Phys. **A494**, 85 (1989).